Geophysical Journal International

Geophys. J. Int. (2013) **194,** 700–718
Advance Access publication 2013 May 9

doi: 10.1093/gji/ggt154

A goal-oriented adaptive finite-element approach for plane wave 3-D electromagnetic modelling

Zhengyong Ren, Thomas Kalscheuer, Stewart Greenhalgh and Hansruedi Maurer

Institute of Geophysics, Department of Earth Sciences, ETH Zurich, Sonneggstr. 5, 8092, *Zurich, Switzerland. E-mail: renzh@aug.ig.erdw.ethz.ch*

Accepted 2013 April 12. Received 2013 April 11; in original form 2012 July 11

SUMMARY

We have developed a novel goal-oriented adaptive mesh refinement approach for finite-element methods to model plane wave electromagnetic (EM) fields in 3-D earth models based on the electric field differential equation. To handle complicated models of arbitrary conductivity, magnetic permeability and dielectric permittivity involving curved boundaries and surface topography, we employ an unstructured grid approach. The electric field is approximated by linear curl-conforming shape functions which guarantee the divergence-free condition of the electric field within each tetrahedron and continuity of the tangential component of the electric field across the interior boundaries. Based on the non-zero residuals of the approximated electric field and the yet to be satisfied boundary conditions of continuity of both the normal component of the total current density and the tangential component of the magnetic field strength across the interior interfaces, three a-posterior error estimators are proposed as a means to drive the goal-oriented adaptive refinement procedure. The first a-posterior error estimator relies on a combination of the residual of the electric field, the discontinuity of the normal component of the total current density and the discontinuity of the tangential component of the magnetic field strength across the interior faces shared by tetrahedra. The second a-posterior error estimator is expressed in terms of the discontinuity of the normal component of the total current density (conduction plus displacement current). The discontinuity of the tangential component of the magnetic field forms the third a-posterior error estimator.

Analytical solutions for magnetotelluric (MT) and radiomagnetotelluric (RMT) fields impinging on a homogeneous half-space model are used to test the performances of the newly developed goal-oriented algorithms using the above three a-posterior error estimators. A trapezoidal topographical model, using normally incident EM waves at both MT and RMT frequencies, is adopted to further test the convergence of the newly developed algorithms against a surface integral approach. Next, the 3D-1 benchmark model from the COMMEMI project is used to show the efficiency of the goal-oriented adaptive algorithm and to compare our solutions against volume integral solutions and other finite-element solutions. For all three test cases, we found that the error estimator using face jumps of normal components of current density embedded in the goal-oriented adaptive refinement procedure shows the most robust performance.

Key words: Numerical solutions; Electromagnetic theory; Magnetotelluric; Magnetic and electrical properties.

1 INTRODUCTION

During the last few decades, plane wave electromagnetic (EM) induction methods have become more and more popular to study the deep structure of the Earth utilizing magnetotelluric (MT) approaches (Chen *et al.* 1996; Nelson *et al.* 1996; Berdichevsky & Dmitriev 2008; Becken *et al.* 2011) and to investigate the shallow subsurface in engineering and environmental applications using the radiomagnetotelluric (RMT) method (Pedersen *et al.* 2006; Tezkan & Saraev 2008; Ismail & Pedersen 2011). The EM field characteristics are determined by the medium properties as well as the frequency. At low frequency, say less than several hundred Hz, the inductive diffusion behaviour of the EM field is dominant, whereas at high frequency, say several tens of thousands of Hz, wave propagation becomes dominant in highly resistive environments. Therefore, the popular practice of directly applying simulation codes

designed to solve the low-frequency MT problem and ignoring the propagation behaviour of the EM field at high frequencies, may be inappropriate (Kalscheuer *et al.* 2008). Consequently, we have developed a new modelling code, which can accurately and efficiently handle both low- and high-frequency situations.

3-D EM modelling is an active research topic in the geophysical community due to its core role in inverting for near-surface structure using EM data. Typically, the simulation methods can be divided into four classes: volume integral methods (Raiche 1974; Hohmann 1975; Weidelt 1975; Avdeev *et al.* 2002; Farquharson *et al.* 2006; Zhdanov *et al.* 2006), surface integral methods (Parry & Ward 1971; Doherty 1988; Liu & Becker 1992; Xu *et al.* 1997; Liu & Lamontagne 1998; Ren *et al.* 2013), finite-difference methods (Mackie *et al.* 1994; Aprea *et al.* 1997; Smith 1996; Haber *et al.* 2000; Newman & Alumbaugh 2002; Hou *et al.* 2006; Streich 2009) and finite-element methods (Badea *et al.* 2001; Mitsuhata & Uchida 2004; Key & Weiss 2006; Nam *et al.* 2007). The advantages and disadvantages of these four methods are compared in the review papers by Avdeev (2005), Boerner (2010) and Everett (2011). In this paper, our method of choice is the finite-element method.

Since the first application of the finite-element method to geoelectromagnetic modelling (Coggon 1971), numerous improvements and further developments have occurred. These include:

(1) Developing proper differential formulations, such as (i) the electric field equation (Nam *et al.* 2007; Farquharson & Miensopust 2011), (ii) the magnetic field equation (Siripunvaraporn *et al.* 2002; Franke *et al.* 2008), (iii) the so-called $H-\phi$ formula (Franke *et al.* 2007) based on the vanishing curl of the magnetic field strength in the air domain under the low-frequency quasi-static approximation, (iv) the $A-\phi$ formula (Haber *et al.* 2000; Badea *et al.* 2001) based on the vanishing divergence of the magnetic field strength, (v) the $T-\Omega$ formula (Mitsuhata & Uchida 2004) based on the vanishing divergence of the total current density, or various combinations of the above;

(2) Obtaining proper expansion functions, such as nodal-based scalar shape functions (Mogi 1996) and curl-conforming edge-based shape functions (Nédélec 1986; Farquharson & Miensopust 2011);

(3) Devising properly discretized meshes, such as structured and unstructured meshes (Key & Weiss 2006; Franke *et al.* 2007);

(4) Improving linear equation solvers (Smith 1996) to quickly and accurately approximate EM fields, such as pre-conditioning techniques to accelerate the convergence rates of iterative solvers and parallel techniques (Zyserman & Santos 2000) to improve solver efficiency;

(5) Finding an optimal distribution of mesh density to improve the accuracy of numerical solutions at low cost, such as the newly developed state-of-the-art adaptive mesh refinement techniques based on global a-posterior error estimators (Key & Ovall 2011; Schwarzbach *et al.* 2011). There are two adaptive refinement approaches, which are the goal-oriented adaptive method and the non-goal–oriented adaptive approach (Oden & Prudhomme 2001). In contrast to so-called non-goal–oriented adaptive refinement strategies, which use global a-posterior error estimators, goal-oriented approaches enforce the efficient refinement of the subdomain in the area of interest, such as domains including the measurement profile. In addition, it allows for global refinement of the mesh density if needed. Therefore, the goal-oriented approach offers an optimal mesh density distribution to ensure accurate solutions.

In this study, we use the electric field equation and check its capability for solving the geoelectromagnetic problem over a wide frequency range. The total electric field is approximated by the lowest order curl-conforming edge-based shape functions and by using unstructured tetrahedral meshes. The OpenMP technique (Chandra 2001) is adopted to assemble and solve in parallel the final system of linear equations. To develop an accurate finite-element code with a low computation cost, the adaptive refinement technique is adopted and is further developed. Only in recent years, the benefits of the adaptive refinement technique were noted by geoelectromagnetic modelling researchers for 2-D MT problems (Key & Weiss 2006; Franke *et al.* 2007) and for 2-D and 2.5-D controlled-source EM problems (Li & Key 2007; Key & Ovall 2011). The successful application of the non-goal–oriented adaptive refinement technique to 3-D controlled-source problems and its performance, were recently reported by Schwarzbach *et al.* (2011). In controlled-source EM problems, the EM field to be approximated around the source is singular if the total field approach is adopted. If the secondary field approach is used, the secondary field in and close to anomalous bodies will still be singular. Therefore, global error estimators designed to decrease the global numerical error and allowing for strongly singular fields caused by physical sources usually offer reasonable numerical solutions (Ren & Tang 2010).

For plane wave EM modelling problems solved by the total field approach where active sources are not considered, it is more efficient to apply the goal-oriented adaptive refinement technique (Oden & Prudhomme 2001). The benefits of the goal-oriented approach have been validated in 2-D and 2.5 D MT and controlled source electromagnetic (CSEM) problems by several authors (e.g. Key & Weiss 2006; Li & Key 2007; Key & Ovall 2011), by using the secondary field approach in which field singularities arise from anomalous bodies. For 3-D plane wave problems using the total field approach, large numbers of unknowns are encountered unless adequate boundary conditions and mesh refinement algorithms are used. Because both artificial refinement techniques and non-goal–oriented adaptive approaches (Franke *et al.* 2007) will lead to dense meshes in some areas which do not contribute to the accuracy of the solutions, the necessity of a goal-oriented adaptive approach becomes more critical.

To drive the goal-oriented adaptive refinement procedure, we propose three residual-based a-posterior error estimators. Since linear curl-conforming shape functions are used to solve the curl–curl electric field equation, the continuity requirements for the normal component of the total current density (**J**) and the tangential component of the magnetic field (**H**) across the interior faces cannot be guaranteed. In addition, the residuals of the electric field over each tetrahedron do not vanish. Therefore, the first error estimator is based on a combination of the volume residuals of the electric field, the face jumps of the normal component of the total current density and the tangential component of the magnetic field strength. The second error estimator is based on jumps in the normal component of the total current density across internal faces, which actually is a measurement of how far the divergence-free condition of the total current density is fulfilled. The third approach is based on the face jumps of the tangential component of the magnetic field, which is a measurement of the basic continuity condition for the magnetic field.

To check the performances of the goal-oriented adaptive refinement algorithms, several numerical experiments were conducted. The numerical experiments not only verify our implementations, but also demonstrate the advantages of the goal-oriented adaptive refinement strategy for 3-D plane wave EM modelling problems over a wide frequency range.

2 PLANE WAVE EM INDUCTION PROBLEM

2.1 Weak formulation of electric field equation

Plane wave geoelectromagnetic induction problems which arise in MT and RMT surveying require the solution of the EM responses in a given bounded computational domain Ω with known tangential components of the magnetic field or the electric field on its surface $\partial\Omega$ (see Fig. 1). Inside this bounded domain, the EM fields ($\mathbf{E}$, $\mathbf{H}$) are controlled by Maxwell's differential equations (Harrington 2001; Jin 2002; Stratton 2007) which in the frequency domain (for time harmonic dependence $\exp^{-i\omega t}$) take the form

$$\nabla \times \mathbf{E} = -\xi \mathbf{H}, \tag{1}$$

$$\nabla \times \mathbf{H} = \chi \mathbf{E}, \tag{2}$$

$$\nabla \cdot (\mathbf{J}_c + \mathbf{J}_d) = 0, \tag{3}$$

$$\nabla \cdot \mu \mathbf{H} = 0, \tag{4}$$

where $\mathbf{E}$ is the electric field strength (V m^{-1}), $\mathbf{H}$ is the magnetic field strength (A m^{-1}), ξ is the impedivity, $\xi = -i\omega\mu$, and χ is the admittivity, $\chi = \sigma - i\omega\epsilon$, μ is the magnetic permeability (V s A m^{-1}), ϵ is the dielectric permittivity (A s V m^{-1}), ω is angular frequency in rad s^{-1}, $\mathbf{J} = \chi\mathbf{E}$ is the total current density flowing through the whole domain Ω including conduction currents ($\mathbf{J}_c = \sigma\mathbf{E}$) and displacement currents ($\mathbf{J}_d = -i\omega\epsilon\mathbf{E}$). The divergence-free condition for the total current density $\mathbf{J}$ in eq. (3) is the continuity equation in a generalized form.

Eliminating the magnetic field strength from Faraday's law (eq. 1) and Ampere's law (eq. 2), we obtain a curl–curl equation for the electric field

$$\nabla \times \frac{1}{\xi}\nabla \times \mathbf{E} + \chi\mathbf{E} = \mathbf{0} \quad \text{in the computational domain} \quad \Omega. \tag{5}$$

To guarantee the uniqueness of the electric field $\mathbf{E}$, the known Neumann type boundary condition (Stratton 2007) for the electric field is enforced on the surface $\partial\Omega$ of the computational domain, which takes the form

$$-\hat{\mathbf{n}} \times \frac{1}{\xi}\nabla \times \mathbf{E} = \mathbf{g}_t \quad \text{on} \quad \partial\Omega, \tag{6}$$

where $\hat{\mathbf{n}}$ is the outward pointing unit normal vector on $\partial\Omega$, $\mathbf{g}_t = \hat{\mathbf{n}} \times \mathbf{H}_0$ and $\mathbf{H}_0$ is the plane wave solution of a half-space model or a multilayered earth model with horizontal layer interfaces.

Taking the vector dot product of eq. (5) with a vector test function $\mathbf{V} \in H(\mathbf{curl}, \Omega)$, applying the first vector Green's identity and integrating by parts (Jin 2002), the equivalent weak formulation of eqs (5) and (6) can be stated thus: Seek $\mathbf{E} \in H(\mathbf{curl}, \Omega)$, $H(\mathbf{curl}, \Omega) = \{\mathbf{V} \in \mathbf{L}^2(\Omega), \nabla \times \mathbf{V} \in \mathbf{L}^2(\Omega)\}$, such that

$$B(\mathbf{E}, \mathbf{V}) = D(\mathbf{V}), \quad \forall \mathbf{V} \in H(\mathbf{curl}, \Omega), \tag{7}$$

where $\mathbf{L}^2$ is the Hilbert vector space of square integrable functions, in which the following inner products are defined:

$$\|\mathbf{v}\|_{L^2,\Omega} = \iiint_\Omega |\mathbf{v}|^2 \, dv, \quad \Omega \subset \mathbb{R}^3,$$

$$\|\mathbf{v}\|_{L^2,F} = \iint_F |\mathbf{v}|^2 \, ds, \quad F \subset \partial\Omega \subset \mathbb{R}^2.$$

$B(,)$ is a self-adjoint symmetric bilinear form and $D()$ is a source inner product term.

$$B(\mathbf{E}, \mathbf{V}) = \iiint_\Omega \frac{1}{\xi}(\nabla \times \mathbf{E} \cdot \nabla \times \mathbf{V} - k^2 \mathbf{E} \cdot \mathbf{V}) \, dv, \tag{8}$$

$$D(\mathbf{V}) = \iint_{\partial\Omega} \mathbf{V} \cdot \mathbf{g}_t \, ds, \tag{9}$$

where k is the complex wavenumber given by $k = \sqrt{-\xi\chi}$.

The entire domain Ω is discretized into a set of tetrahedral elements $\mathcal{T} = \bigcup_{n=1}^{N_t} \mathcal{T}_n \subseteq \Omega$, $1 \le n \le N_t$, N_t is the total number of tetrahedra. The lowest order vector Nédélec shape function (Nédélec 1986) is used to obtain an approximate solution $\mathbf{E}_h \in \mathcal{H}(\mathbf{curl}, \mathcal{T})$ of the electric field in eq. (7) on unstructured meshes. Here, $\mathcal{H}(\mathbf{curl}, \mathcal{T})$ is the finite-element space with lowest order vector Nédélec shape functions. For more detail of the finite-element approximation, please see Appendix A. Once the electric field $\mathbf{E}_h \in \mathcal{H}(\mathbf{curl}, \mathcal{T})$ is obtained, we use the post-processing procedure presented in Appendix C to compute more interesting variables, such as apparent resistivities, phases and vertical magnetic transfer functions.

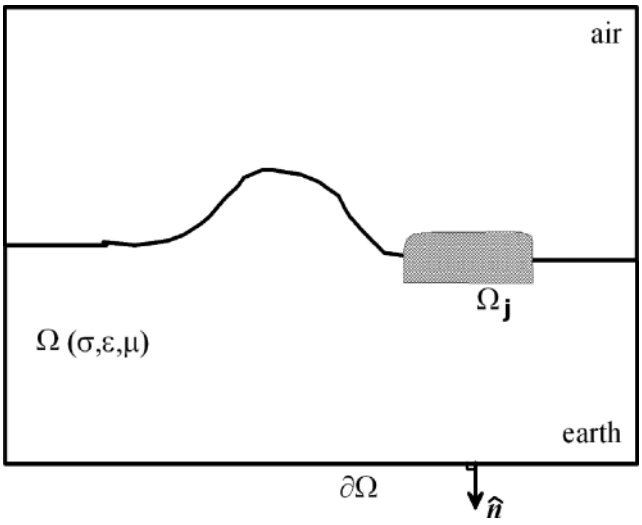

Figure 1. Illustration of the geometrical domain Ω (including both air and Earth) for the electromagnetic induction problem. Here, $\partial\Omega$ is the boundary and $\hat{\mathbf{n}}$ is its unit normal vector pointing out of Ω. The subdomain Ω_j contains the measuring profile on the air–Earth interface and, hence, is the domain of interest.

2.2 Error sources of $\mathbf{E}_h \in \mathcal{H}(\mathbf{curl}, \mathcal{T})$

The numerical error sources involved in solving for the electric field $\mathbf{E}_h \in \mathcal{H}(\mathbf{curl}, \mathcal{T})$ can be classified as follows. The first error source arises from the model set-up and the mesh discretization of complicated models entailing curved surfaces. This includes: (i) the sizes of the surfaces of the computational domain Ω which is normally required to have its boundaries several skin depths from the anomalous bodies, (ii) the size of each tetrahedron which needs to be less than one skin depth so that the assumption of a linear variation of the electric field is approximately guaranteed, (iii) the quality of each tetrahedron and (iv) how closely the curved surfaces for geometrically complicated models are approximated. The second error source arises from inaccurately solving the final system of equations (A3). To avoid the above two error sources, first high-quality unstructured meshes are used. The mesh quality is generated by enforcing the 'radius-to-edge' ratio for each tetrahedron to be no more than 1.4. (Rücker *et al.* 2006; Si 2006; Ren & Tang

2010). The distance of the surface $\partial\Omega$ to the anomalous bodies is about 5–10 skin depths. Then, besides using analytical forms for volume integrals of the vector products containing Nédélec vector shape functions (see eq. A2) in constructing the system matrix $\mathbf{A}$ (see Appendix A), a multicore parallel direct LU solver PARDISO (Schenk & Gärtner 2004) via Intel MKL C library (Intel 2010) is used to accurately yield the solutions.

The third error source is due to the use of the curl-conforming space $\mathcal{H}(\mathbf{curl}, \mathcal{T})$ to solve for the electric field. In the curl-conforming space $\mathcal{H}(\mathbf{curl}, \mathcal{T})$ (using the lowest order Nédélec elements), although the divergence-free condition of the total current $\mathbf{J}$ is satisfied within each tetrahedron, the strong differential equation form for the electric field is relaxed to its weak (integral) formulation and only the continuity of the tangential component of the electric field is satisfied. The residual of the strong differential formulation is not strictly equal to zero, which is equivalent to a residual volume current density $\mathbf{J}_{\mathrm{r}_e}$. This non-zero volume current density generates an additional magnetic field according to the Biot–Savart law (Stratton 2007). The continuity of the normal component of the total current across the interior faces is not satisfied; and the tangential continuity of the magnetic field $\mathbf{H}$ across these faces is not satisfied. The jumps in the normal component of the total current density are equivalent to the generation of an additional interface charge density ρ. Using Coulomb's law (Stratton 2007), these falsely accumulated surface charges ρ generate an additional electric field, which is denoted by $\mathbf{E}_\rho$. The jumps in the tangential component of the magnetic field strength can be explained as falsely accumulated surface electric currents $\mathcal{J}$ which generate an additional magnetic field according to the Biot–Savart law denoted by $\mathbf{H}_\mathcal{J}$ (Stratton 2007). Then, both the electric field $\mathbf{E}_h$ and the magnetic field $\mathbf{H}_h$ can be updated as

$$\mathbf{E}_h \Longleftarrow \mathbf{E_h} - \mathbf{E}_\rho, \tag{10}$$

$$\mathbf{H}_h \Longleftarrow \mathbf{H_h} - \mathbf{H}_\mathcal{J} - \mathbf{H}_{\mathbf{J}_{\mathrm{r}_e}}. \tag{11}$$

The first approach of using the divergence correction for the electric field in eq. (10) was adopted by Smith (1996) and Farquharson & Miensopust (2011), who showed that great acceleration of the convergence rate of iterative solvers was achieved. Without this divergence correction, iterative solvers show very slow convergence rate and struggle to compute correct forward modelling solutions (Farquharson & Miensopust 2011). In our study, we used a direct matrix solver to solve the system of linear equations. We show that a robust direct solver has the capability of offering accurate solutions for both MT and RMT models. Therefore, the divergence correction is not needed or adopted in our study.

For the following discussion, we define the residual of the electric field $\mathbf{E}_h \in \mathcal{H}(\mathbf{curl}, \mathcal{T})$ as

$$\mathbf{r}_\mathrm{e} = \nabla \times \frac{1}{\xi} \nabla \times \mathbf{E}_h + \chi \mathbf{E}_h. \tag{12}$$

For linear Nédélec shape functions and elements with constant impedivity ξ, the curl–curl term on the right of eq. (12) vanishes.

The direct divergence correction for the electric field (eq. 10) or the magnetic field (eq. 11) might be still questionable. Although the erroneously accumulated surface electric charges or currents can be kept to a minimum level, the residuals $\mathbf{r}_\mathrm{e}$ of the electric field $\mathbf{E}_h \in \mathcal{H}(\mathbf{curl}, \mathcal{T})$ might be increasing so that the resultant magnetic field contains increasing errors by the last term in eq. (11). Then, the Galerkin orthogonality property of the vanishing integral of the dot product of the residual of the electric field $\mathbf{r}_e$ and the vector Nédélec shape functions $\mathbf{N}_i$ in eq. (A2) over the tetrahedra $\mathcal{T}_n$ supporting $\mathbf{N}_i$ is no longer valid, that is,

$$\iiint_{\mathcal{T}_n} \mathbf{N}_i \cdot \mathbf{r}_\mathrm{e} \, \mathrm{d}v \neq 0. \tag{13}$$

This inequality will to some extent break down the equivalence of the solutions between the strong differential equation form given by eqs (5) and (6) and its weak formulation given in eqs (7) and (A1) for simple models having continuous material parameters. For complicated models with discontinuities of material parameters across interfaces between elements, additional continuity conditions (discussed in Section 3) have to be enforced. Therefore, the optimal approach of improving the accuracy of $\mathbf{E}_h$ appears to be to simultaneously decrease the numerical errors arising from the non-zero residuals and falsely accumulated surface electric charges and currents, which is implemented in the following goal-oriented adaptive refinement algorithm, accounting for the continuity conditions.

3 A-POSTERIOR ERROR ESTIMATORS

Over an interior face F, which is shared by two tetrahedra $\mathcal{T}_i$ and $\mathcal{T}_j$, having unit normal vector $\hat{\mathbf{n}}_F$ pointing from $\mathcal{T}_i$ to $\mathcal{T}_j$, we denote the finite-element solutions of the EM field in $\mathcal{H}(\mathbf{curl}, \mathcal{T})$ on the sides of $\mathcal{T}_i$ and $\mathcal{T}_j$ by $\mathbf{E}_-$ and $\mathbf{H}_-$, and $\mathbf{E}_+$ and $\mathbf{H}_+$ over the face, respectively. The continuity conditions for the electric field and the magnetic field yield

$$\nabla \cdot \mathbf{J} = 0 \Rightarrow \nabla \cdot \chi \mathbf{E} = 0, \quad \hat{\mathbf{n}}_F \cdot (\chi_- \mathbf{E}_- - \chi_+ \mathbf{E}_+) = 0, \tag{14}$$

$$\hat{\mathbf{n}}_F \times (\mathbf{E}_- - \mathbf{E}_+) = \mathbf{0}, \tag{15}$$

$$\nabla \cdot \mathbf{B} = 0 \Rightarrow \nabla \cdot \mu \mathbf{H} = 0, \quad \hat{\mathbf{n}}_F \cdot (\nabla \times \mathbf{E}_- - \nabla \times \mathbf{E}_+) = 0, \tag{16}$$

$$\hat{\mathbf{n}}_F \times \left(\frac{1}{\xi_-} \nabla \times \mathbf{E}_- - \frac{1}{\xi_+} \nabla \times \mathbf{E}_+ \right) = \mathbf{0}. \tag{17}$$

Define $[\cdot]_F$ as the L^2 difference norm operator cross the shared face, then, we have

$$[\hat{\mathbf{n}} \cdot \mathbf{J}]_F = \sqrt{\iint_F |\hat{\mathbf{n}} \cdot (\chi_- \mathbf{E}_- - \chi_+ \mathbf{E}_+)|^2 \, \mathrm{d}s}, \tag{18}$$

$$[\hat{\mathbf{n}} \times \mathbf{E}]_F = \sqrt{\iint_F |\hat{\mathbf{n}} \times (\mathbf{E}_- - \mathbf{E}_+)|^2 \, \mathrm{d}s}, \tag{19}$$

$$[\hat{\mathbf{n}} \cdot \mathbf{B}]_F = \sqrt{\iint_F |\hat{\mathbf{n}} \cdot (\nabla \times \mathbf{E}_- - \nabla \times \mathbf{E}_+)|^2 \, \mathrm{d}s}, \tag{20}$$

$$[\hat{\mathbf{n}} \times \mathbf{H}]_F = \sqrt{\iint_F |\hat{\mathbf{n}} \times \left(\frac{1}{\xi_-} \nabla \times \mathbf{E}_- - \frac{1}{\xi_+} \nabla \times \mathbf{E}_+ \right)|^2 \, \mathrm{d}s}. \tag{21}$$

According to the physical behaviour of the EM fields in each tetrahedron having constant electrical parameters, both the electric field and magnetic field should be divergence-free and both of them should satisfy the constraints of the continuity conditions across the internal surfaces. We note that $\mathbf{E}_h$ belongs to $\mathcal{H}(\mathbf{curl}, \mathcal{T})$, such that the divergence-free condition for the electric field inside each element is satisfied (refer to eq. 3). Then according to Faraday's law, inside each element, the divergence-free condition for the magnetic field is also satisfied, $\nabla \cdot \mathbf{B}_h = \frac{1}{\mathrm{i}\omega} \nabla \cdot \nabla \times \mathbf{E}_h \equiv 0$, since

$\nabla \cdot \nabla \times \equiv 0$. The tangential component of the electric field is continuous across the interior surface F. This leads to $[\hat{\mathbf{n}} \times \mathbf{E}]_F = 0$. Furthermore, note that $\hat{\mathbf{n}}_F \cdot \nabla \times \mathbf{E} = -\nabla \cdot (\hat{\mathbf{n}}_F \times \mathbf{E})$, therefore, $[\hat{\mathbf{n}} \cdot \mathbf{B}]_F = 0$. However, the continuity of the normal component of the total current density $\mathbf{J}$ and the continuity of the tangential component of the magnetic field $\mathbf{H}$ cannot be guaranteed in the $\mathcal{H}(\mathbf{curl}, \mathcal{T})$ space. The approach of evaluating the conformity to these continuity conditions naturally offers a means to estimate the numerical errors of the finite-element approximations and can be used to guide the mesh refinement procedure to reduce these amplitude discontinuities.

First, we construct an a-posterior error estimator ($\eta^e_{\mathcal{T}_n}$, which is named as *error estimator rJH*) for a given tetrahedron $\mathcal{T}_n$ in terms of the volume residuals for the electric field and the required continuity constraints on the normal component of the total current density and the tangential component of the magnetic field across surfaces F of the tetrahedron $\mathcal{T}_n$, that is,

$$\left[\eta^e_{\mathcal{T}_n}\right]^2 = h^2_{\mathcal{T}_n} \|\mathbf{r}_e\|^2_{L^2,\mathcal{T}_n} + \frac{1}{2} h_F \left\{[\hat{\mathbf{n}} \cdot \mathbf{J}]^2_F + [\hat{\mathbf{n}} \times \mathbf{H}]^2_F\right\}. \tag{22}$$

Here, F is redefined as the union of four triangles enclosing the tetrahedron $\mathcal{T}_n$, h_F stands for the maximum diameter of each triangle in F (especially the last term in eq. 22 is to be understood as the sum over all four faces of $\mathcal{T}_n$), $h_{\mathcal{T}_n}$ is the maximum diameter of the tetrahedron $\mathcal{T}_n$. The factor 1/2 comes from the fact that the residuals/jumps on the faces F of the tetrahedra are shared by two elements and the factors h_F and $h_{\mathcal{T}_n}$ arise from the Helmholtz decomposition theory of $\mathcal{H}(\mathbf{curl}, \mathcal{T})$ (Beck *et al.* 2000). The first term refers to the effect of the extra volume current density though the whole tetrahedron generated by inaccurate numerical solutions $\mathbf{E}_h$. The second term stands for the contribution of incorrect surface charges accumulated through discontinuous currents through the surfaces. The third term takes account of fictitious surface electric currents due to discontinuous tangential magnetic fields. This a-posterior error estimator is consistent with that presented by other authors (e.g. Chen *et al.* 2007) which is obtained by multiplying eq. (22) by the factor of $\xi_0 = -\mathrm{i}\omega\mu_0$. For the high-contrast scenarios of geophysical applications (such as at the air–Earth interface), the dominant error term in eq. (22) could be the second term which measures the jump of the normal component of the electric current density across faces. While the L^2 norm of this quantity scales like $O((\sigma_- - \sigma_+)^2)$, its energy norm (which was used by Beck *et al.* 2000) scales like $O((\sigma_- - \sigma_+))$. This difference might make the above L^2 norm error estimator in eq. (22) more efficient than its energy norm variation.

In terms of the amount of additionally accumulated charges and currents on the surfaces, we define two further a-posterior error estimators for the electric field. The first (which is named as *error estimator J*) is

$$\left[\eta^e_{\mathcal{T}_n}\right]^2 = \frac{1}{2}[\hat{\mathbf{n}} \cdot \mathbf{J}]^2_F, \tag{23}$$

and the second (which is named as *error estimator H*) is

$$\left[\eta^e_{\mathcal{T}_n}\right]^2 = \frac{1}{2}[\hat{\mathbf{n}} \times \mathbf{H}]^2_F. \tag{24}$$

In the above two error estimators, the factor h_F is dropped so that we can directly estimate the absolute amount of falsely accumulated surface charges and currents, respectively. Using Coulomb's law (Stratton 2007), the accumulated surface charges generate an additional electric field. The accumulated surface electric currents generate an additional magnetic field according to the Biot–Savart law (Stratton 2007). Therefore, these two error estimators without the scaling factor h_F are consistent with the measurements of unsatisfied physical behaviour of the EM fields. It avoids an underestimation or an overestimation of errors that occurs on small or large faces, respectively, if the scaling factor h_F is considered.

4 GOAL-ORIENTED ADAPTIVE REFINEMENT

4.1 Error in the quantity of interest

In geophysical EM surveying, the measuring profiles are usually located on the air–Earth interface. We are particularly interested in the accuracy of the electric and magnetic fields, or apparent resistivities and phases, in the subsurface surrounding the measuring sites. It is well known from classical error analysis theory of the finite-element method (Brenner & Scott 2008), that once the global mesh density satisfies a certain level, the accuracies of the finite-element solutions are strongly affected by the local mesh density. This suggests that global refinement techniques might not only increase the number of unknowns and hence the computational cost, but also they may not efficiently improve the accuracy of numerical solutions. To seek an optimal balance between computational cost and numerical accuracy, our interest focuses on local refinement of the elements surrounding the profiles, so that solution accuracy can be improved in subdomains of practical interest.

The goal-oriented adaptive refinement concept (Oden & Prudhomme 2001) is an ideal method to satisfy our above interest. Instead of globally decreasing errors of the electric fields, it targets decreasing the error of a linear functional $L(\mathbf{E})$ of the local electric field, cooperating with the dual/adjoint bilinear form $B^*(,)$ of the original weak formulation $B(,)$ for the electric field $\mathbf{E}$. We define this linear functional of the electric field as $L(\mathbf{E})$, $\mathbf{E} \in H(\mathbf{curl}, \Omega)$ ($\mathbf{E}$ is the accurate solution of the electric field). Hence, we construct the dual weak form to the primary weak form (eq. 7), which seeks to find $\mathbf{W} \in H(\mathbf{curl}, \Omega)$, such that

$$B^*(\mathbf{W}, \mathbf{V}) = L(\mathbf{V}), \quad \forall \mathbf{V} \in H(\mathbf{curl}, \Omega),$$

where $B^*(,)$ is the adjoint operator of the bilinear form $B(,)$. Due to the self-adjoint property of $B(,)$, $B^*(,)$ is equal to $B(,)$. The solution $\mathbf{W}$ of the above dual problem is usually referred to as the 'influence function' (Oden & Prudhomme 2001). Then, considering the primary weak formulation given by eq. (7), the weak variational form of $\mathbf{W}$ becomes

$$B(\mathbf{W}, \mathbf{V}) = L(\mathbf{V}). \tag{25}$$

In analogy to eq. (A1), the finite-element approximation $\mathbf{W}_h$ of $\mathbf{W}$ is defined as $\mathbf{W}_h \in \mathcal{H}(\mathbf{curl}, \mathcal{T})$ such that

$$B(\mathbf{W}_h, \mathbf{V}_h) = L(\mathbf{V}_h), \quad \forall \mathbf{V}_h \in \mathcal{H}(\mathbf{curl}, \mathcal{T}). \tag{26}$$

Now, we turn our attention to the numerical error analysis of $L(\mathbf{E})$. Let $\mathbf{e}$ denote the numerical error of the electric field, then,

$$L(\mathbf{e}) = L(\mathbf{E} - \mathbf{E}_h), \quad \mathbf{e} \in H(\mathbf{curl}, \Omega). \tag{27}$$

Using eq. (25),

$$\begin{aligned} L(\mathbf{e}) &= B(\mathbf{W}, \mathbf{e}) = B(\mathbf{W}_h + \mathbf{w}, \mathbf{e}) \\ &= B(\mathbf{W}_h, \mathbf{e}) + B(\mathbf{w}, \mathbf{e}) \\ &= B(\mathbf{w}, \mathbf{e}), \end{aligned} \tag{28}$$

where $\mathbf{w}$ is the error of $\mathbf{W}$, and due to $\mathbf{W}_h \in \mathcal{H}(\mathbf{curl}, \mathcal{T})$, $\mathbf{e} \in H(\mathbf{curl}, \Omega)$, the Galerkin orthogonality property (Brenner & Scott 2008) yields $B(\mathbf{W}_h, \mathbf{e}) = 0$.

Using eq. (8), the explicit form of $B(\mathbf{e}, \mathbf{w})$ is

$$B(\mathbf{e}, \mathbf{w}) = \iiint_{\Omega} \frac{1}{\xi}(\nabla \times \mathbf{e} \cdot \nabla \times \mathbf{w} - k^2 \mathbf{e} \cdot \mathbf{w})\, \mathrm{d}v,$$

where $\mathbf{w}$ and $\mathbf{e}$ are the expressions for the numerical errors. Now, we define an error indicator for $L(\mathbf{e})$, using the Cauchy–Schwartz inequality (Oden & Prudhomme 2001; Brenner & Scott 2008)

$$|L(\mathbf{e})| = |B(\mathbf{e}, \mathbf{w})| \leqslant \sum_{n=1}^{N_\mathrm{t}} |B_{\mathcal{T}_n}(\mathbf{e}, \mathbf{w})|$$

$$\leqslant \sum_{n=1}^{N_\mathrm{t}} \|\mathbf{e}\|_{e,\mathcal{T}_n} \|\mathbf{w}\|_{e,\mathcal{T}_n} \approxeq \sum_{n=1}^{N_\mathrm{t}} \mathcal{C}_n \|\mathbf{e}\|_{L^2,\mathcal{T}_n} \|\mathbf{w}\|_{L^2,\mathcal{T}_n}, \tag{29}$$

where $\mathcal{C}_n$ is a positive constant number which depends on the mesh size, impedivity ξ and admittivity χ, and $\|\cdot\|_e$ is the energy norm in terms of the bilinear form $B(,)$, with its definition as $\|\cdot\|_e = \sqrt{|B(,)|}$. To avoid the difficulty of evaluating errors in the energy norms (f as to $\|\mathbf{e}\|_{e,\mathcal{T}_n}$, the true solution of the electric field $\mathbf{E}$ is unknown so it is impossible to evaluate the terms $\nabla \times \mathbf{e} \cdot \nabla \times \mathbf{e}$ and $\mathbf{e} \cdot \mathbf{e}$ in $B(,)$ over each element $\mathcal{T}_n$) and to still maintain the efficiency of error estimation, we replace the energy norm by its equivalent L^2 norm (Zdunek & Rachowicz 2005), which can be easily and efficiently evaluated in terms of the error estimators defined in eqs (22)–(24). Denote $\eta^e_{\mathcal{T}_n} = \|\mathbf{e}\|_{L^2,\mathcal{T}_n}$ as the element error indicator for $\mathbf{E}$ and $\eta^w_{\mathcal{T}_n} = \|\mathbf{w}\|_{L^2,\mathcal{T}_n}$ for $\mathbf{W}$, then the error estimator for $L(\mathbf{e})$ is

$$\eta_L = \sum_{n=1}^{N_\mathrm{t}} \eta^e_{\mathcal{T}_n} \eta^w_{\mathcal{T}_n}. \tag{30}$$

4.2 Boundary value problem for the dual problem

In the dual weak form of eq. (25), $L(\mathbf{V})$ is a linear functional of an arbitrary function $\mathbf{V} \in H(\mathbf{curl}, \Omega)$. In geoelectromagnetic modelling problems, we are interested in the accuracy of the electric field ($\mathbf{E} \in H(\mathbf{curl}, \Omega)$) around the profiles. Hence, a reasonable form for the linear functional could be

$$L(\mathbf{E}) = \sum_{j=1}^{t} \frac{1}{V_j} \iiint_{\Omega_j} \mathbf{E} \cdot \mathbf{I} \mathrm{d}v. \tag{31}$$

Here, $L(\mathbf{E})$ denotes the averaged electric field over t subdomains Ω_j of interest (see Fig. 1), which contain the measuring profiles and V_j denotes the volume of the jth subdomain Ω_j. Taking the variation of the weak form of eq. (25) and considering the above definition, we can recover the differential boundary value problem for $\mathbf{W}$ in the dual problem as

$$\nabla \times \frac{1}{\xi} \nabla \times \mathbf{W} + \chi \mathbf{W} = -\sum_{j=1}^{t} \frac{\Upsilon_j \mathbf{I}}{V_j} \quad \text{in} \quad \Omega, \tag{32}$$

$$-\hat{\mathbf{n}} \times \frac{1}{\xi} \nabla \times \mathbf{W} = \mathbf{0} \qquad \text{on} \quad \partial\Omega, \tag{33}$$

where $\mathbf{I} = [1, 1, 1]$ is a vector of unit elements which acts as a vector source injected into each tetrahedron of each subdomain of interest (see Fig. 1), and Υ_j is the characteristic function which is 1 over the entire subdomain Ω_j.

From a physical point of view, the vector function $\mathbf{W}$ (in eqs 32 and 33) can be considered as the generalized electric field Green's function due to the injection of a set of vector sources with the homogeneous Neumann boundary condition. The correctness of enforcing the homogeneous Neumann boundary condition of eq. (33) is easily validated. To obtain the error indicator η_L (eq. 30) of $L(\mathbf{e})$, we need only consider the difference between the accurate and the numerical solutions. We could use any other boundary condition if it can guarantee the existence and uniqueness of $\mathbf{W}$, because we do not care about the real distribution of the influence function, as long as it puts emphasis on the numerical errors of the solutions in the subdomains of interest. It can be realized that this generalized Green's function $\mathbf{W}$ varies rapidly over the subdomains containing the profiles, due to the artificially injected unit vector sources $\mathbf{I}$. Similar to the point sources used in direct current resistivity surveying, $\mathbf{W}$ surrounding these domains changes significantly, which definitely leads to rather large numerical errors. Therefore, the element error indicator $\eta^w_{\mathcal{T}_n}$ for $\mathbf{W}$ in these domains can be rather large compared to those in other domains and enlarges the element error indicator $\eta^e_{\mathcal{T}_n}$ of the electric field in a weighting approach by using eq. (30).

Hence, artificially increasing the element error indicator $\eta^w_{\mathcal{T}_n}$ in subdomains of interest is physically equivalent to introducing artificial sources within the confines of these subdomains. Furthermore, as evident from eqs (28) and (29), local numerical errors of the linear functional $L(\mathbf{e})$ over certain subdomains of interest are propagated over the whole computational domain and are influenced by the global numerical errors of both the electric field and the generalized Green's function $\mathbf{W}$. This is why the generalized Green's function $\mathbf{W}$ is referred as the 'influence function'. The approximation of the influence function is listed in Appendix B.

4.3 Fully automatic refinement algorithm

With the availability of the above element error estimators for the electric field and for the influence field, η_L can be easily approximated using the relationship in eq. (30). Here, we define a global relative error estimator as

$$r^L_\eta = \frac{\eta_L}{|L(\mathbf{E}_h)|}. \tag{34}$$

It should be noted that we have replaced the energy norm by its equivalent L^2 norm which is scaled by a positive factor $\mathcal{C}_n$ ($n = 1, \ldots, N_\mathrm{t}$) for each tetrahedron to evaluate the above η_L in eq. (30). Therefore, we cannot expect this global relative error estimator to be a rather small number. However, r^L_η should decrease during the mesh refinement procedure, which is actually observed in our numerical experiments.

The goal-oriented adaptive refinement strategy can be described by the following four-step process:

(1) Given a mesh $\mathcal{T} = \bigcup_{n=1}^{N_\mathrm{t}} \mathcal{T}_n$ of Ω, a maximum number of unknowns and a maximum number of iterations, compute the finite-element approximations $\mathbf{E}_h$ of the electric field and $\mathbf{W}_h$ of the influence field. Estimate the element error indicators $\eta^e_{\mathcal{T}_n}$ and $\eta^w_{\mathcal{T}_n}$ and also the relative error indicator r^L_η by using eqs (34) and (30).

(2a) If r^L_η is not less than a given small positive tolerance $\complement$ (such as 10^{-2}), the number of unknowns on the mesh $\mathcal{T}_n$ is less than the given maximum number and the current iteration number is less than the given maximum number, then search the array of element error indicators and mark the tetrahedra with error indicators $\eta^{\mathcal{T}_n}_L = \eta^e_{\mathcal{T}_n} \eta^w_{\mathcal{T}_n}$ satisfying

$$\frac{\eta^{\mathcal{T}_n}_L}{\max(\eta^{\mathcal{T}_n}_L)} = \beta_n > \beta, \quad 0 < \beta < 1, \tag{35}$$

where β_n is the relative element error indicator and β is a threshold value which controls the number of refined elements. Then, generate a new mesh by dividing the volumes of the marked elements by a

factor of 2 by the Delaunay refinement approach (Si 2006), replace the old mesh $\mathcal{T}_n$ by the new mesh and go back to step (1).

(2b) If $r_\eta^L < \complement$ or the maximum number of unknowns or iterations is reached, stop the refinement procedure and go to step (3).

(3) Compute the magnetic field from the electric field using Faraday's law in eq. (1). Compute the vertical magnetic transfer functions (VMTFs) and the impedance tensor as described in Appendix C.

Using the a-posterior error estimators *rJH*, *J* and *H* defined in eqs (22), (23) and (24), respectively, and the above fully automatic refinement scheme, seven different mesh refinement strategies are proposed as follows:

- *Global mesh refinement*: Do not estimate a-posterior errors estimators and in step (2a), simply divide the volumes of all $\mathcal{T}_n$ by a factor of 2.
- *Non-goal–oriented approach rJH*: Use *error estimator rJH* in eq. (22) to estimate $\eta_{\mathcal{T}_n}^e$ in eq. (30). Do not solve the dual problem to compute $\eta_{\mathcal{T}_n}^w$ in eq. (30) (which is equal to setting $\eta_{\mathcal{T}_n}^w = 1.0$), that is, base the mesh refinement entirely upon the set of $\eta_{\mathcal{T}_n}^e$.
- *Non-goal–oriented approach J*: Similar to *Non-goal–oriented approach rJH*, but using *error estimator J* in eq. (23) to estimate $\eta_{\mathcal{T}_n}^e$ in eq. (30) (setting $\eta_{\mathcal{T}_n}^w = 1.0$).
- *Non-goal–oriented approach H*: Similar to *Non-goal–oriented approach rJH*, but using *error estimator H* in eq. (24) to estimate $\eta_{\mathcal{T}_n}^e$ in eq. (30) (setting $\eta_{\mathcal{T}_n}^w = 1.0$).
- *Goal-oriented approach rJH*: Use *error estimator rJH* in eq. (22) to estimate $\eta_{\mathcal{T}_n}^e$ and $\eta_{\mathcal{T}_n}^w$, that is, base the mesh refinement upon $\eta_L^{\mathcal{T}_n}$.
- *Goal-oriented approach J*: Use *error estimator J* in eq. (23) to estimate $\eta_{\mathcal{T}_n}^e$ and $\eta_{\mathcal{T}_n}^w$.
- *Goal-oriented approach H*: Use *error estimator H* in eq. (24) to estimate $\eta_{\mathcal{T}_n}^e$ and $\eta_{\mathcal{T}_n}^w$.

The numerical solutions for the E_x^p source polarization are used to estimate the a-posterior errors for the electric field, $\eta_{\mathcal{T}_n}^e$ in eq. (30) in the following experiments. Numerical solutions for the H_x^p source polarization can also be used to estimate the a-posterior errors. It might yield better performance than the E_x^p source polarization, because fields of the H_x^p source polarization may be less smooth than fields of the E_x^p source polarization. Therefore, both options are offered in our implementation. For a given mesh, three linear systems sharing the same system matrix have to be solved, where two linear systems arise from these two source polarizations and one linear system is for the influence field. Therefore, once the LU decomposition of the system matrix for the primary problems involving the E_x^p or H_x^p sources polarization is achieved, the extra cost to compute the influence field is relatively inexpensive.

5 NUMERICAL EXPERIMENTS

We have implemented the above algorithms in a stand-alone C++ code which is derived within the framework of a freely downloadable 3-D direct current adaptive finite-element method code (Ren & Tang 2010). The linear nodal Lagrange elements of the direct current resistivity forward solver are replaced by the linear vector edge-based elements (Nédélec 1986; Jin 2002) and the iterative solvers are replaced by the direct sparse matrix solver PARDISO (Schenk & Gärtner 2004). The mesh refinement and generation are accomplished by directly calling the open source package TetGen (Si 2006). The slices of mesh density and element error estimator distributions are visualized by the open visualization software Paraview (Henderson *et al.* 2004). The computation platform is a PC with Intel(R) Xeon(TM) CPU 3.20 GHz (four cores) and 32.0 GB RAM.

5.1 Comparison with analytical solutions

First, a half-space model at two frequencies of 10 Hz and 300 kHz is investigated. The resistivity of the air space is set to $10^{16}\Omega$m. The magnetic permeability and the dielectric permittivity are the free space values. A total of 51 measuring sites is located with equidistant spacing along the *y*-axis. For this model, the numerical errors arise only from improper mesh discretization. During the goal-oriented and non-goal–oriented adaptive mesh refinement procedures, elements with relative error indicators $\beta_n > 0.01$ are selected to be refined for the next step. The adaptive iteration is terminated when the number of unknowns exceeds 1.5 million. On this model, the solutions of the EM field are regular (non-singular), therefore the non-goal–oriented adaptive strategies might not have the capability to focus on locally refining the subdomains of interest that enclose the measurement profile.

5.1.1 MT case

The frequency is 10 Hz, the resistivity of the homogeneous Earth structure is $10^2\,\Omega$m, the computational domain is $\Omega = [-10\,\text{km}, 10\,\text{km}]^3$, with sites located in $y = [-500\,\text{m}, 500\,\text{m}]$. The plane wave is normally incident (angle of incident from vertical $= 0^\circ$) on the horizontal ground surface. Plots of relative and absolute errors for apparent resistivities and phases, respectively, versus the numbers of unknowns (degrees of freedom) of the above mesh refinement strategies are shown in Fig. 2. Due to the usage of linear curl-conforming shape functions, the expected theoretical quasi-optimal slope of the convergence rate on a log–log plot is $-1/3$ for the global mesh refinement technique and non-goal–oriented adaptive mesh refinement techniques (Chen *et al.* 2007). Not surprisingly, the non-goal–oriented adaptive refinement algorithms (Franke *et al.* 2007; Ren & Tang 2010; Schwarzbach *et al.* 2011) show poor convergence rates which are even worse than the global refinement technique. The reason is that the non-goal–oriented algorithms are mainly focused on refining the global mesh density and try to decrease the global numerical error. In fact, the poor performances of these non-goal–oriented adaptive refinement algorithms are consistent with their theoretical behaviour (Beck *et al.* 2000; Chen *et al.* 2007) which were designed to automatically decrease the global numerical error. Although the numerical solutions at this level are still inaccurate, we believe that they will improve if we allow the adaptive refinement procedures to continue to levels where the mesh densities in subdomains both including and excluding the measuring sites are dense enough. Their quasi-optimal convergence rates would then show the standard log–log slope of $-1/3$.

In Fig. 2, we also present the error curves of the three goal-oriented adaptive refinement strategies. The *goal-oriented approach rJH* shows a log–log convergence rate slightly less than $-1/3$ at the beginning and then it quickly adjusts its behaviour after three iterations. Unlike *goal-oriented approach rJH*, *goal-oriented approach H* quickly reaches the quasi-optimal slope of $-1/3$, and starting with the second iteration at 84 967 unknowns, the slope is steeper than $-1/3$. The most efficient performance is obtained with *goal-oriented approach J*. Starting from the initial model, super-optimal log–log slopes in the range of $-1/2$ to -1.0 are obtained which means that the numerical errors decrease linearly or quadratically

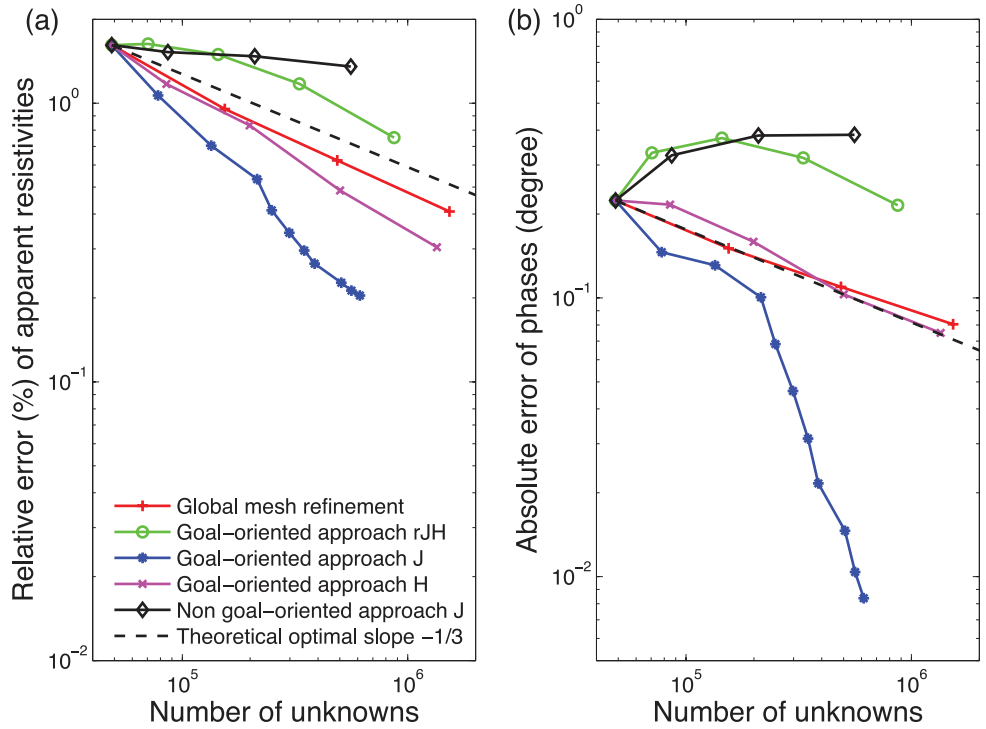

Figure 2. Errors of apparent resistivities (a) and phases (b) in terms of different mesh refinement strategies for the half-space model at a frequency of 10 Hz and for the E_x^p source polarization. Similar errors were obtained for the H_x^p source polarization but were omitted here. Due to the similar behaviour of the non-goal–oriented approaches *rJH*, *J* and *H*, only results for *non-goal–oriented approach J* are shown. The dashed black lines give the theoretically obtainable optimal convergence curves of the global mesh refinement and non-goal–oriented adaptive mesh refinement techniques (for problems with singular geometries and fields, Chen *et al.* 2007).

with the number of unknowns. We should note that in the 11th iteration, the number of unknowns of *goal-oriented approach J* is less than 0.7 million, yet it can still offer highly accurate solutions compared to all other mesh refinement strategies. Between two iterations, the number of added elements slightly decreases while dramatically improving the accuracy of the numerical solutions.

To see the details of mesh refinement procedures, we compare in Fig. 3 mesh densities and the relative element error indicators β_n (defined in eq. 35) at the fourth iteration for the *global mesh refinement*, *goal-oriented approach J* and *non-goal–oriented approach J*. In Fig. 3, for comparison purposes, the relative element error indicators β_n are computed in terms of both $\eta^e_{\mathcal{T}_n}$ and $\eta^w_{\mathcal{T}_n}$ for these three approaches, though the global refinement approach does not require computation of β_n and β_n of the non-goal–oriented approach normally is computed with $\eta^w_{\mathcal{T}_n} = 1.0$. Starting with the initial mesh of 7044 nodes and 40 255 elements, the globally refined mesh (Figs 3a and b) which decreases the element volume of the initial mesh by a factor of $(1/2)^3$ has 209 788 nodes, 1 305 855 elements and 1 531 497 edges (unknowns). We observe that the elements are globally refined for elements both close to and far away from the subdomain of interest which includes the profile region marked by a white rectangle. Departures of this solution from the analytic expressions are 0.41 per cent relative error for the apparent resistivies and 0.08° absolute error for the phases which are close to those of the solution at the fourth iteration for *goal-oriented approach J* with involves fewer unknowns, only 14 per cent of those used in the globally refined mesh. The resulting mesh and the relative element error estimator distribution of the fourth iteration for *goal-oriented approach J* are shown in Fig. 3(c). Unlike the global mesh refinement algorithm, this error estimator efficiently identifies the subdomains of interest. This includes the white rectangular region. The method refined the elements inside this region. A local view for the whole domain marked by the white rectangle is shown in Fig. 3(d). At the same time, its error estimator performed correctly in identifying other subdomains in need of refinement. For instance, we can see that the discretization of the air space was not dramatically refined. Because of the low frequency 10 Hz used in this model, the EM field varies only slightly and therefore, the approximate condition of less than 0.1 wavelength for the side lengths of the tetrahedra to obtain accurate solutions with linear curl-conforming shape functions is easily satisfied. Similarly, for subdomains below ground that are at a distance of five to six times the skin depth from the measuring sites, the amplitudes of the fields are close to zero so that their variations can be ignored.

In Figs 3(e) and (f), we show the global view and the local view, respectively, of the mesh densities at the plane $x = 0$ on the fourth mesh for *non-goal–oriented approach J*. There are 77 041 nodes, 475 524 elements and 558 943 edges (unknowns) in Fig. 3(e). The relative errors of these numerical solutions are 1.35 per cent for the apparent resistivies and of 0.77 per cent for the phases. Compared to *goal-oriented approach J*, this inferior solution which entails a denser mesh indicates that a large number of extra elements added to subdomains far away from the domain of interests (white rectangle) actually do not contribute to the accuracy of the numerical solution on the profile. For subdomains including the profile (shown in Fig. 3f), the elements are not refined enough (compared to the local view of mesh density in Fig. 3d) so that the accuracy of the solution is not dramatically improved. This is a sacrifice in computational efficiency by globally densening the mesh. This phenomenon actually is consistent with the theoretical error population (Brenner & Scott 2008) of the finite-element method, which states that once the global mesh density reaches a certain level,

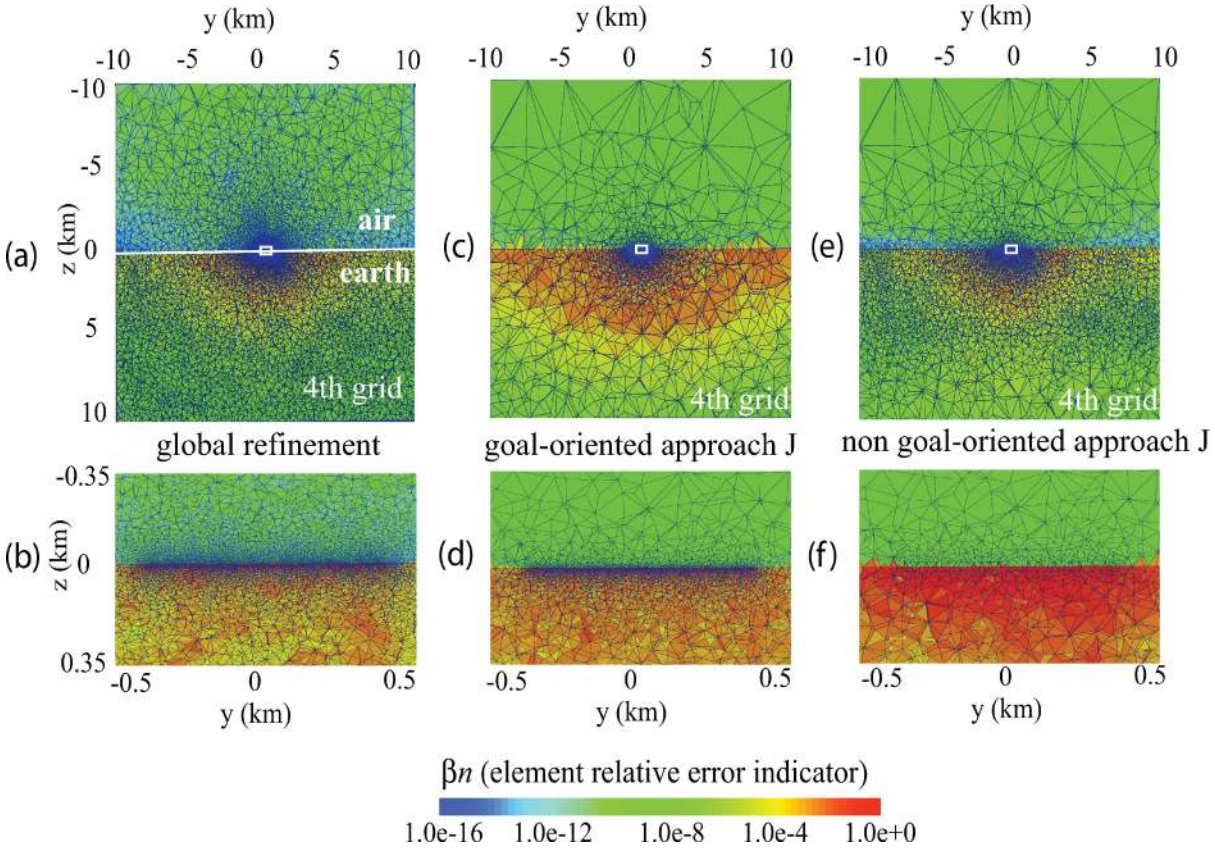

Figure 3. Illustration of mesh densities at slice $x = 0$ for the half-space model at a frequency of 10 Hz. The panels (a) and (b) in the left-hand column show global and local expanded views of the fourth grid generated by the global refinement approach. The panels (c) and (d) show distributions of the element relative error indicator β_n on the fourth grid generated by *goal-oriented approach J*, where panel (d) is a local view of the white rectangle marked in (c). The right-hand panels (e) and (f) are for *non-goal–oriented approach J*. For comparison, the relative element error indicators β_n are computed in terms of both $\eta^e_{T_n}$ and $\eta^w_{T_n}$ for these three approaches.

the accuracies of numerical solutions at special subdomains are strongly dependent on the local mesh densities in these special subdomains. This error population theory acts in basic support of our goal-oriented adaptive refinement strategies, which try to redistribute the global mesh density to achieve an optimal accuracy and then focus on locally refining the mesh density in the subdomains of interest.

5.1.2 RMT case with an oblique incidence angle

We now consider the RMT case in which frequency is 300 kHz, the resistivity of the homogeneous Earth is 30 000 Ωm, the computational domain is $\Omega = [-1\text{ km}, 1\text{ km}]^3$, with receiver sites located in $y = [-50\text{ m}, 50\text{ m}]$. The plane wave is obliquely incident on the flat air–Earth interface at an inclination angle of 60° from the z-axis and an azimuthal angle of 0° from the x-axis. Due to small wavelengths, the starting mesh discretization is generated by enforcing the spatial constraints of side lengths of 0.5 wavelength in each tetrahedron. Curves showing the relative and absolute errors for apparent resistivities and phases, respectively, versus the number of unknowns for the above mesh refinement strategies are given in Fig. 4. Similar observations can be made as for case 1. In the H_x^p polarization case, the normal component of the total current density $\mathbf{J}_\text{n}$ at the Earth side does not vanish due to galvanic leakage (Berdichevsky & Dmitriev 2008). On the air–Earth interface, the normal component of the total current density needs to be continuous due to the divergence-free condition of total current density $\nabla \cdot \mathbf{J} = 0$. To measure how the divergence-free condition is satisfied in our computation, we compute the relative error of the numerical discontinuity of $\mathbf{J}^0_\text{n} - \mathbf{J}^1_\text{n}$, where $\mathbf{J}^0_n$ is the normal component of total current density at the air side and $\mathbf{J}^1_\text{n}$ is the normal component of total current density at the Earth side. The result is shown in Fig. 5. The convergence of these relative errors shows the ability of the algorithm to recognize and adjust for the galvanic leakage phenomena.

5.2 Comparison with boundary element method (BEM) solutions for a topographic hill model

5.2.1 MT case

As a second example, the trapezoidal hill model of Nam *et al.* (2007) at a frequency of 2 Hz is considered. Due to the effect of the 3-D topographical surface, the electric field should be weakly singular at the corners. Therefore, this model should provide a good performance test of the above adaptive strategies to deal with singular field cases. Accurate solutions of this model are available from a surface integral approach (Ren *et al.* 2013), which can be utilized as the reference solutions. The size of the hilltop square is 450 m × 450 m, the size of the square base is 2000 m × 2000 m and the height of this hill is 450 m. A geometrical approximation is made to cut off the horizontally infinite Earth–air interface into a finite square of size 40 km × 40 km. The resistivity of the

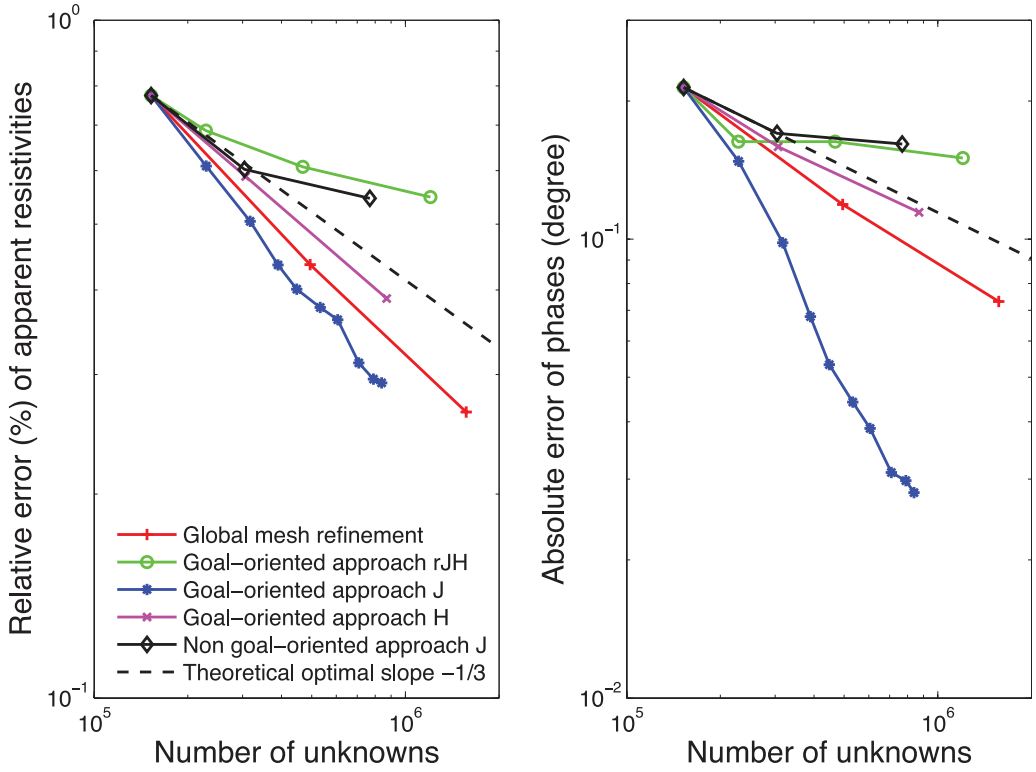

Figure 4. Errors at a frequency of 300 kHz and for plane waves obliquely incident on the air–Earth interface at an angle of 60° from the z-axis.

Earth is 100 Ωm; the di-dielectric permittivity of the Earth is ε_0 and its magnetic permeability is μ_0. The resistivity of the free space is 10^{16} Ωm. 19 sites along the y-axis are arranged at equidistant spacing over the interval $y = [-1500\,\text{m}, 1500\,\text{m}]$. The purpose of this example is to distinguish the performances of the three goal-oriented approaches. The starting mesh discretization is generated by enforcing the spatial constraints of side lengths of 1.0 wavelengths in each tetrahedron, which results in 34 588 unknowns. The obtained parameters on the seventh mesh refinement are listed in Table 1, as well as the average residuals compared to surface integral solutions. *Goal-oriented adaptive approach J*, shows the most robust performance. At the seventh mesh refinement, it needs the lowest number of unknowns of all tested approaches but still has excellent agreement with the surface integral solution. The mesh contains only 104 344 edges (unknowns) which is just 12.7 per cent of the unknowns used by *goal-oriented adaptive approach rJH* and 18.0 per cent of the unknowns used by *goal-oriented adaptive approach H*.

Local views of the mesh densities and the element relative error indicator β_n of *goal-oriented approach J* for a slice at $x = 0$ across the topographical hill are shown in Fig. 6. All elements with $\beta_n > \beta = 0.05$ are identified to be refined in the next iteration. We compare three meshes, the starting mesh, the third mesh and the seventh mesh, with their results shown in Figs 7 and 8. First, neither the air domain nor the subdomains far away from the topographical hill or below the ground surface are refined densely. The reason is similar to that for the half-space model. Since the frequency of just 2 Hz is rather low, the quasi-static approximation is valid in this example, since displacement currents are negligible. The variations of the EM fields in both air and Earth domains are not dramatic. Therefore, the approximate condition of 0.1 skin depth of the EM field for the side lengths of each tetrahedron in these two domains is easily satisfied. For subdomains containing the profiles, due to the large contrast of the conductivities between the air and the Earth and the introduction of the singular unit sources inside these subdomains in the dual problem, all local subdomains enclosing the measuring sites are efficiently refined, especially for the endpoints of the profile.

To carefully check the performance of *goal-oriented approach J*, we present in Figs 7 and 8 the horizontal electric and magnetic fields, as well as apparent resistivities and phases, from the starting mesh, and the meshes of the third and the seventh iterations. In Fig. 7, we observe that there are large differences in the solutions of the three meshes for the y-component of the electric field of the H_x^p polarization, but only slight differences for the x-component of the electric field of the E_x^p polarization. The reason is that $E_y^{H_x^p}$ is singular at the corners due to charge accumulation. Therefore, sufficiently dense meshes are required to correctly treat this singular behaviour. The correct convergence behaviour observed in Fig. 7(b) once again validates the goal-oriented adaptive scheme using *a posterior error estimator J*. At sites close to the two endpoints of the profile, the magnetic fields for the starting mesh and for the third iteration mesh have relatively large differences compared to the reference solutions. The reason is that the magnetic fields are computed by Faraday's law (eq. 1), and to obtain highly accurate solutions, dense meshing is required in these two subdomains. Thanks to the idea from the goal-oriented approach of introducing singular sources inside these subdomains, the final E and H solutions converge to the reference solutions. *Goal-oriented adaptive approach J* also successfully forces the apparent resistivities and phases to converge (see Fig. 8) to the reference solutions at relatively low cost, especially at the endpoints, which is a challenge for the other strategies. Similar convergence behaviour of the z-component of the magnetic fields of the E_x^p polarization and the y-component of the VMTF (T_y) can be observed in Fig. 9 (due to the symmetry of the profile and the hill model, $H_z^{H_x^p} = 0$ and $T_x = 0$).

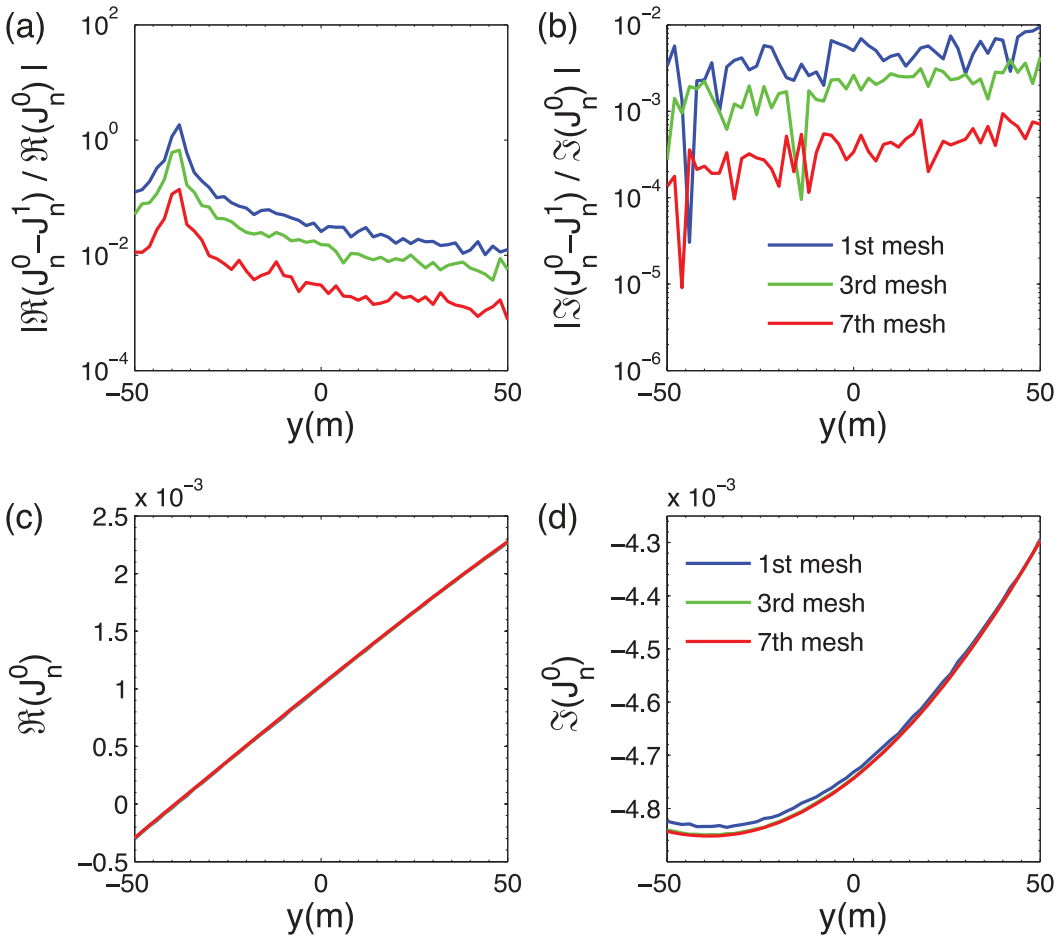

Figure 5. The relative errors of the real [panel (a)] and imaginary [panel (b)] parts of the discontinuity of the normal component of the total current density $\mathbf{J}_n$ across the air–Earth interface in the H_x^p polarization for a half-space model with a 60° incidence angle and at a frequency of 300 kHz, in terms of *goal oriented approach J*. $\mathbf{J}^0$ and $\mathbf{J}^1$ are the total current density at the air and Earth side, respectively. The number of unknowns for each refinement is shown in Fig. 4. The real part errors are larger than the imaginary component errors, but decrease with increasing mesh density, and are typically less than 1 per cent for the seventh mesh. The error jumps at several points in the imaginary part arise from the relocation of tetrahedrons around the RMT sites during in the mesh regeneration. This phenomenon was also observed in the 2-D case (Key & Weiss 2006; Li & Key 2007). The real [panel (c)] and imaginary parts [panel (d)] of $\mathbf{J}_n^0$ are also shown. Owing to the oblique incidence, $\Re(\mathbf{J}_n^0)$ has a zero crossing at $y \approx -40$ m and $\Im(\mathbf{J}_n^0)$ obtains its maximum amplitude there. This explains the smaller relative errors in the imaginary part and the trends of the errors along the profile.

Table 1. Parameters of the mesh discretization of the three goal-oriented approaches for the trapezoidal hill model of Nam *et al.* (2007) at a frequency of 2 Hz. In the adaptive refinement procedure, elements with $\beta_n > 0.05$ (in eq. 35) are marked to be refined. The residuals of the apparent resistivities and phases obtained by three goal-oriented approaches are given with respect to the reference solutions obtained by the surface integral approach (Ren *et al.* 2013).

Method	Mesh level	No. elements	No. edges	Average residual			
				ρ_a^{xy} (Ωm)	ρ_a^{yx} (Ωm)	ϕ_a^{xy} (°)	ϕ_a^{yx} (°)
Goal-oriented approach rJH	7	953 218	1 107 619	1.45	3.80	0.16	0.16
Goal-oriented approach J	7	88 698	104 344	1.58	3.62	0.09	0.09
Goal-oriented approach H	7	500 201	580 996	1.26	3.71	0.10	0.09

5.2.2 RMT case

Here, we investigate a model involving high frequency (100 kHz) and high resistivity, such as arises in RMT where displacement currents can be important. The plane wave is vertically incident along the z-axis. The model is rescaled from the trapezoidal hill model (Nam *et al.* 2007; Ren *et al.* 2013) used in our second numerical experiment. The computational domain is $\Omega = [-1\,\text{km}, 1\,\text{km}]^3$. The resistivity of the Earth is 10 kΩm; the di-dielectric permittivity of the Earth is $5\varepsilon_0$ and the magnetic permeability is μ_0. This combination of electrical properties may, for instance, be representative of weakly fractured granite. The resistivity of the free space is 10^{16} Ωm. A total of 53 station sites is distributed at equal distance along the y-axis between $y = [-150\,\text{m}, 150\,\text{m}]$. Due to the high frequency, the variation of waves in both the air and the Earth is dramatic, therefore, careful mesh discretization with high node density is required. Spatial dimensions of less than 1.0 wavelengths in each tetrahedron are initially enforced, which generates a rather dense mesh with 221 280 elements and 265 095 edges (unknowns). *Goal-oriented approach J* is used to simulate this challenging model. The reference solutions are from the semi-analytical surface integral approach on a highly dense surface mesh computed by the

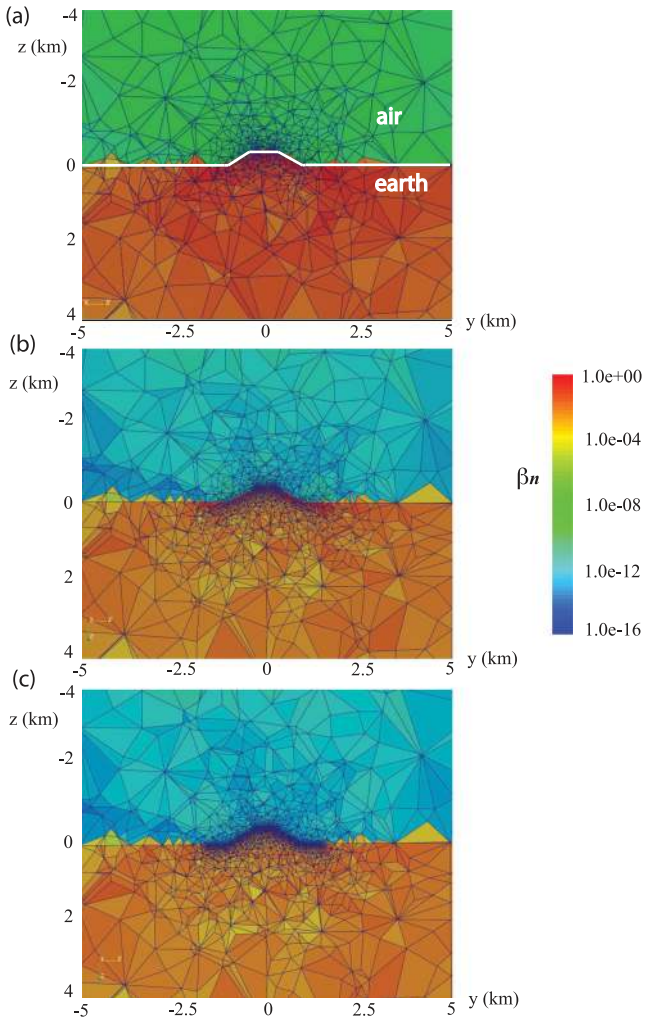

Figure 6. Illustration of the element relative error indicator β_n (defined in eq. 35) and local mesh densities for a slice at $x = 0$ through the trapezoidal hill model at a frequency of 2 Hz for *goal-oriented approach J*. Panel (a) is the starting model, (b) is the third mesh and (c) is the seventh mesh.

adaptive multilevel fast multipole boundary element method (Ren *et al.* 2013).

We show the relative element error indicators β_n in Fig. 10. Elements with $\beta_n > \beta = 0.01$ are marked for refinement in the next iteration. Unlike the previously presented low-frequency case, large numbers of elements in the air space are identified by their relative element error estimators for refinement in the next iteration. In the high-frequency examples, the air space has serious influence on the accuracies of solutions, because the presence of displacement currents dramatically decreases the wavelength as compared to that of the quasi-static approach. Hence, careful mesh discretization must be considered in the air space. The element relative error indicators β_n of subdomains under the ground, which are far away from the topographical surface and are at sufficiently large depth, are rather small, which is consistent with the nearly vanishing amplitudes of the EM waves in such regions due to induction phenomena. For the sixth mesh, the numerical solutions in a local coordinate system (x, t, n) along the profile are presented in Fig. 11. The vertical component n is in the direction normal to the topography and the tangential component t is along the topography of the profile. The component x is perpendicular to the profile direction and also follows the air–Earth interface. The adaptively refined solutions are clearly convergent to the surface integral solutions. A discussion on the physical behaviour of transfer functions and EM field components in the local coordinate system is given in Ren *et al.* (2013).

Apart from the excellent agreement between our adaptive goal-oriented finite-element method solutions and the surface integral solutions, we also observe the singular behaviour of the electric field across topographic changes of slope in the conductivity model for the H_x^p polarization if we increase the mesh density of corner regions. For the H_x^p source polarization, the y-components of the electric fields are singular at the topographic corners, due to the accumulation of surface charges on these positions. These singularities lead to large differences of 0.5–1.0 orders of magnitude in the amplitudes of the field components (predominantly in the electric field) and are consistent with the analytical behaviour of waves at high frequencies (Olyslager 1994, 1995).

5.3 Comparison with 3-D benchmark numerical solutions

The 3D-1 model (shown in Fig. 12) is a benchmark test model which was analysed within the COMMEMI project (Zhdanov *et al.* 1997). It comprises a resistive homogeneous background Earth with an embedded conductive prism. The depth to the top surface of the prism is 250 m. The resistivity of the air space is 10^{16} Ωm, the resistivity of the background Earth ρ_1 is 100 Ωm and the resistivity of the prism ρ_2 is 0.5 Ωm. Both the dielectric permittivity and magnetic permeability of the Earth are the same as the free space values. A total of 62 measuring sites is located at equal spacing along the x-axis in the range $x = [-3000\,\text{m}, 3000\,\text{m}]$. We compare our numerical solutions with those of other approaches, that is, the solutions from the COMMEMI project, the $T - \Omega$ finite-element solutions on structured meshes (Mitsuhata & Uchida 2004) and the divergence-correction finite-element method (Farquharson & Miensopust 2011) using the curl–curl electrical field equation and structured meshes. Instead of applying direct divergence correction of the total current density after several iterations (Farquharson & Miensopust 2011), our approach focuses on increasing mesh density where there are significant jumps of the normal components of the total current density, while keeping the Galerkin orthogonality, which is a basic condition for the existence and uniqueness of a finite-element solution in the curl-conforming space.

The first test frequency is 0.1 Hz. The computational domain is $\Omega = [-70\,\text{km}, 70\,\text{km}]^3$ containing an air layer with a height of 70 km. The starting model which has spatial dimensions of less than 1.0 wavelength for each tetrahedron, involves 30 835 elements and 36 789 edges. Here, we use the optimal *goal-oriented approach J* to compare against other solutions. A threshold value of $\beta = 0.05$ is specified in the refinement procedure. As for the above two experiments, the *goal-oriented approach J* again refines the mesh density of subdomains of interest, with the number of elements and edges slowly increasing. We compare the solutions obtained on the starting mesh, the 15th mesh and the 20th mesh (with mesh discretization listed in Table 2). First, since our solutions are symmetrical along the profile, only half of the profile needs to be shown in Fig. 13. Due to the coarse mesh density of the starting mesh, its solution has large differences compared to our FEM solutions of the other meshes. When the adaptive refinement procedure is applied, the goal-oriented algorithm automatically detects the large discrepancies at the measuring sites right above the centre of the conductive prism where the current density and the EM fields are sharply varying. For the 15th mesh, involving 154 572 tetrahedra, both apparent resistivities (Figs 13a and b) and phases (Figs 13c

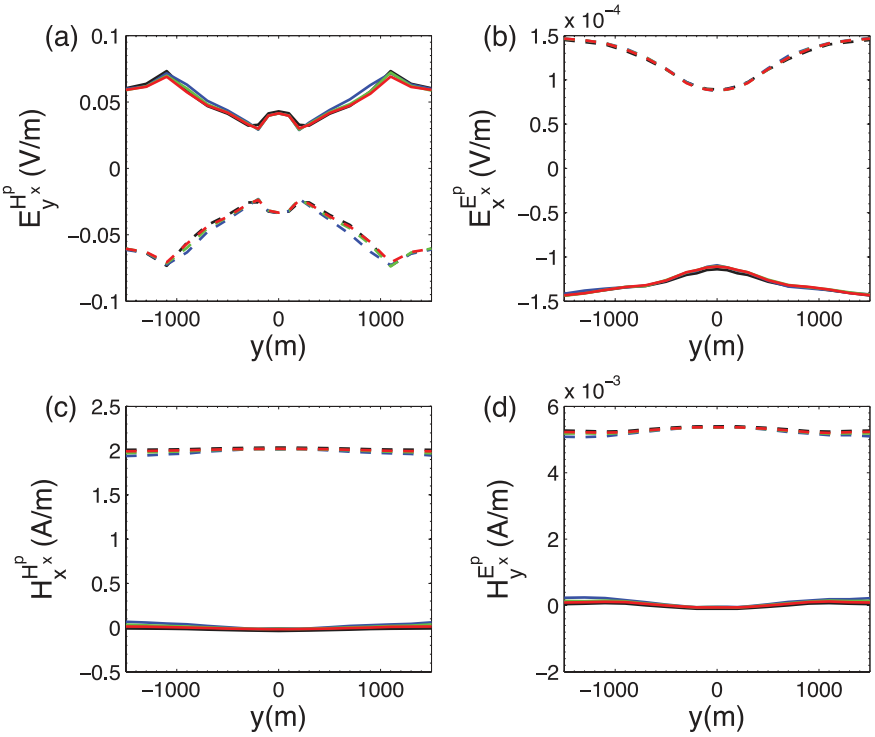

Figure 7. Horizontal electric fields of the H_x^p polarization (a) and the E_x^p polarization (b) as well as the horizontal magnetic fields of the H_x^p polarization (c) and the E_x^p polarization (d) obtained using *goal-oriented approach J*, compared to the surface integral solutions (reference solutions) of the trapezoidal hill model at a frequency of 2 Hz. The black curves are obtained by the surface integral method (Ren *et al.* 2013). The blue curves represent solutions on the initial mesh, the green curves are solutions on the third mesh and the red curves are solutions on the seventh mesh. The solid lines are the real part of the field and the dashed lines are the imaginary parts of the field.

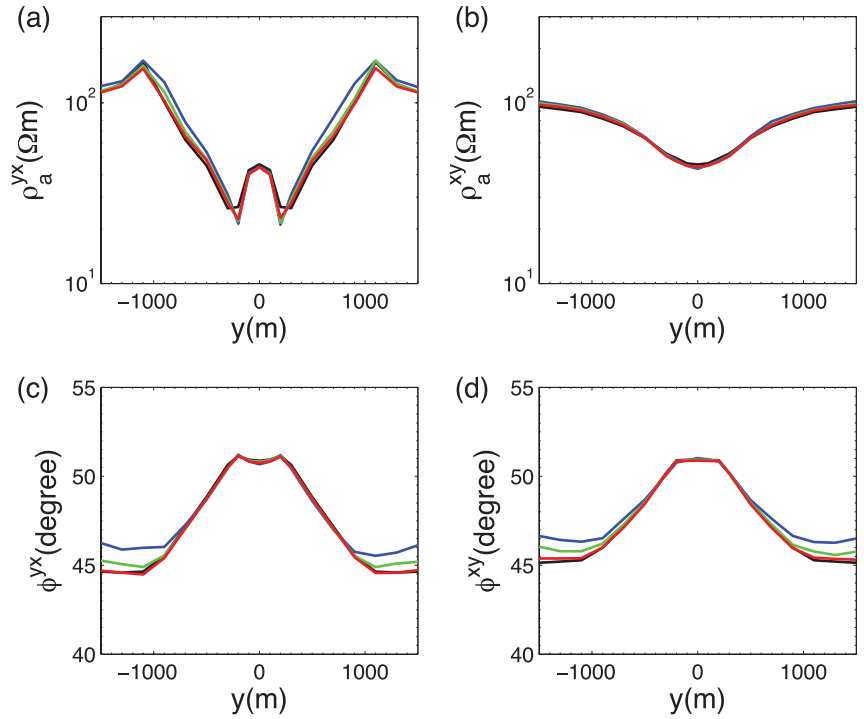

Figure 8. Apparent resistivities (a and b) and phases (c and d) obtained through *goal-oriented approach J*, and compared to the surface integral solutions of the trapezoidal hill model at a frequency of 2 Hz. The black curves are obtained by the surface integral approach (reference solutions of Ren *et al.* 2013). The blue curves represent solutions of the initial mesh, the green curves are for solutions of the third mesh and the red curves are solutions of the seventh mesh.

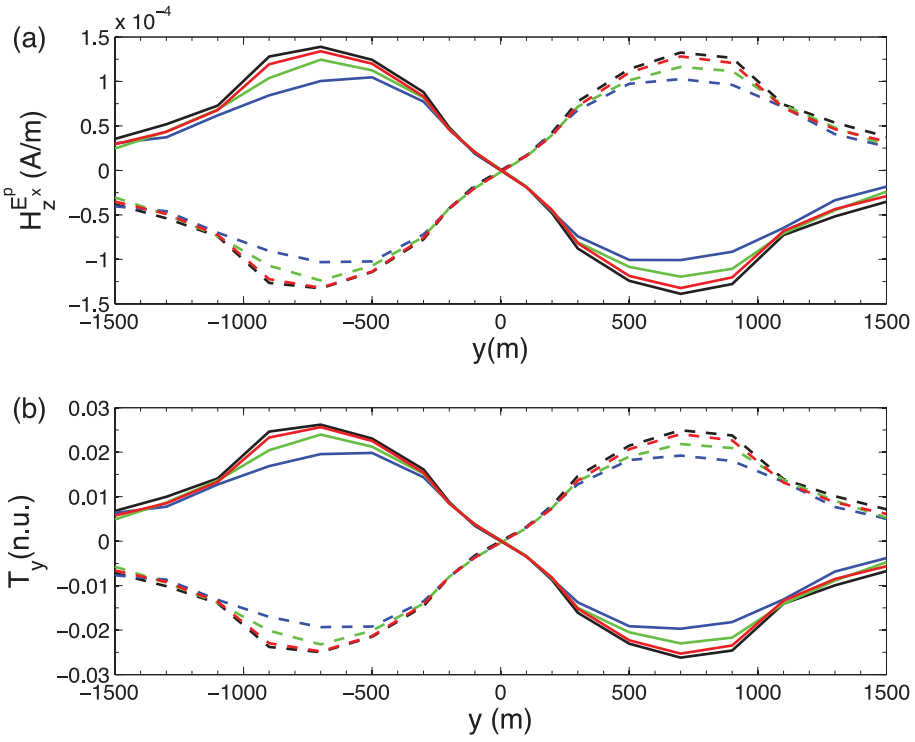

Figure 9. The z-component of the magnetic field of the E_x^p polarization (a) and the y-component of the VMTF (b) obtained through *goal-oriented approach J*, which are compared to the surface integral solutions of the trapezoidal hill model at a frequency of 2 Hz. The black curves are obtained by the surface integral approach (reference solutions of Ren *et al.* 2013). The blue curves represent solutions of the initial mesh, the green curves are for solutions of the third mesh and the red curves are solutions of the seventh mesh. The real parts are denoted by the dashed lines and the imaginary parts by the solid lines.

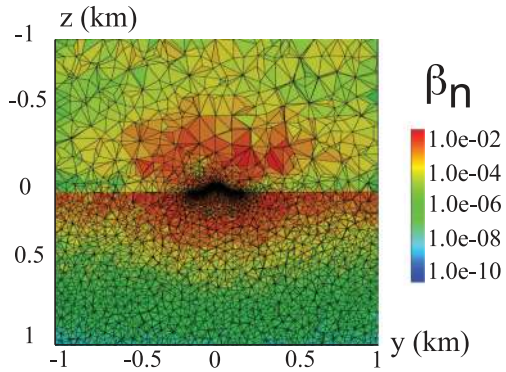

Figure 10. Illustration of the relative element error indicator β_n and the local mesh densities for a slice at $x = 0$ for the trapezoidal hill model at a frequency of 100 kHz. Computed for the sixth mesh of *goal-oriented approach J*. Elements with $\beta_n > 0.01$ are to be refined in the next iteration of the adaptive mesh refinement.

and d) show good agreement with the reference solutions of Zhdanov *et al.* (1997), Mitsuhata & Uchida (2004) and Farquharson & Miensopust (2011). In particular, our solutions have better agreement with the approach of Farquharson & Miensopust (2011) which uses more unknowns (elements). In the 20th mesh (results are not shown here), generated with our refinement algorithm where the number of unknowns is 245 128, solutions are very close to those of the 15th mesh, which implies relative convergence to the accurate solution. It should be noted that using a lesser number of unknowns, the $T - \Omega$ approach obtained quite good results. This is because the $T - \Omega$ approach which makes the quasi-static assumption explicitly enforces the condition of $E_{\rm n} = 0$ at the air–Earth interface, where $E_{\rm n}$ is the normal component of the electric field on the Earth side. However, this assumption is not valid for high-frequency cases where displacement currents must be considered.

Similar results are obtained at a frequency of 10 Hz (in Table 2 and Fig. 14), where $\Omega = [-7\,\text{km}, 7\,\text{km}]^3$ contains an air layer with a thickness of 7 km. In Fig. 14, only the solution of the 10th mesh is shown. The solution of the 15th mesh (not shown) is quite close to the solution of the 10th mesh. This might imply that our solution shown in Fig. 14 can be trusted.

For the 3D-2 model from the COMMEMI project (Zhdanov *et al.* 1997), we also obtained excellent results. They are given in a supplementary file of this paper.

6 CONCLUSIONS

We have successfully developed and reported on a novel goal-oriented adaptive finite-element scheme for plane wave EM modelling. The applicability of the curl–curl electric field equation over a wide frequency band is established utilizing curl-conforming shape functions and unstructured grids. Therefore, a new accurate and efficient 3-D code for plane wave problems such as low-frequency MT problems and high-frequency RMT problems is available. It has the capability to automatically improve the accuracy for complicated problems involving curved subsurface interfaces and topographic surfaces.

In our goal-oriented approach, four parameters control the goal-oriented adaptive mesh refinement strategies: the threshold value $\mathtt{C}$ for the global relative error estimator, the maximum number of unknowns, the maximum permissible number of iterations and the threshold value β for the relative element error indicators. Indeed, the global relative error estimator r_η^L cannot be less than a rather small threshold $\mathtt{C}$, although the values of r_η^L decrease when the

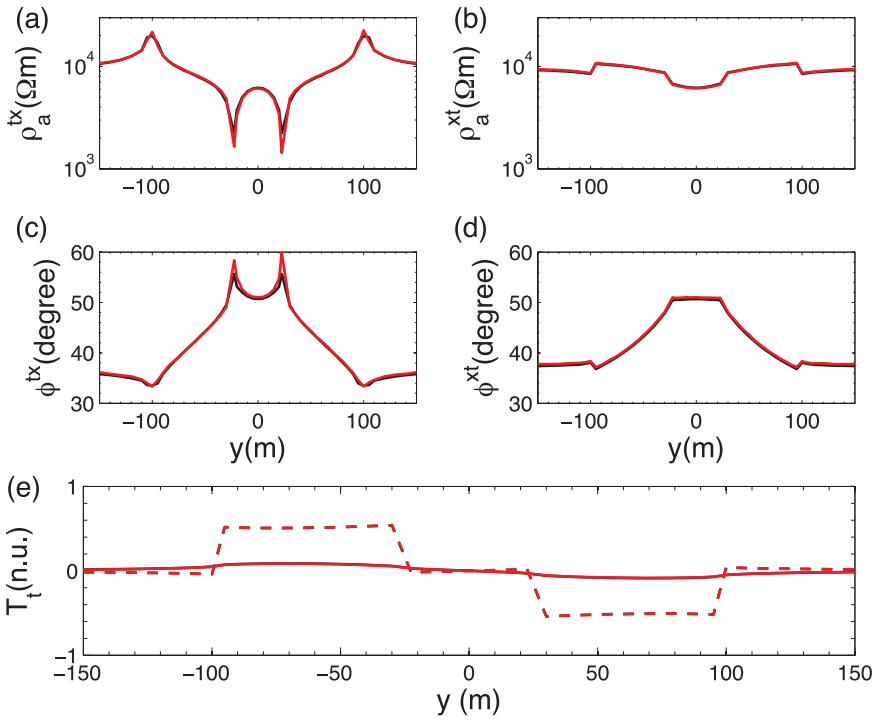

Figure 11. Comparison of apparent resistivities (a and b), phases (c and d) and VMTF (T_t, (d)) obtained with the *goal-oriented approach J* on the sixth adaptively refined FEM mesh, compared to surface integral solutions of Ren *et al.* (2013) for the trapezoidal hill model at a frequency of 100 kHz in a local coordinate system, where *t* is the direction along the profile. The black curves are obtained by the surface integral method. The red curves are solutions on the sixth mesh. In panel (e), the solid curves are the real parts of T_t and the dashed curves are its imaginary parts.

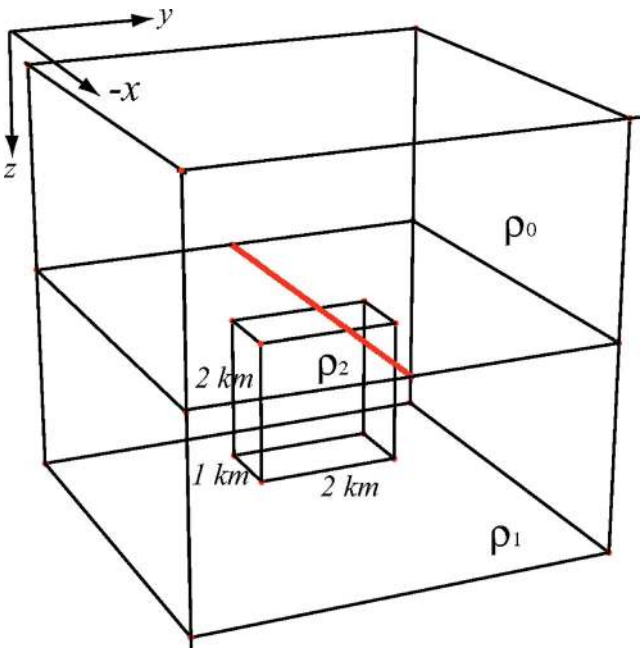

Figure 12. Illustration of the benchmark 3D-1 model with measuring sites along a profile (marked in red) parallel to the *x*-axis on the flat air–Earth interface.

adaptive strategies are applied. Therefore, the most practically useful stopping criterion is the maximum number of unknowns, which is dependent on the computer hardware. The accuracies of all the solutions shown in this study, while very good, can be further improved as soon as more powerful computational resources become available. Based on our experiments, a good option for the choice of β is to mark a subset of elements with large error indicators so that the per cent ratio of these marked elements to the total elements is about 1–5 per cent.

Based on our experiments, the advantages of goal-oriented adaptive approaches over the global refinement method and non-goal–oriented adaptive approaches are clearly evident. In addition, the performances of the three a-posterior error estimators were evaluated in the framework of the goal-oriented adaptive approach, and all three can offer acceptable convergence rates. We observed that the *error estimator rJH* has inferior performance compared to the error estimators *J* and *H*. The reason is that the residual of the electric current density within an element is dominant in the *error estimator rJH*. Since geophysical EM problems normally involve large contrasts of conductivities, *a-posterior error estimator J* based on the continuity condition of the normal component of the total current density exhibits the most effective performance. Therefore, it might be the most desirable error estimator for geophysical EM modelling problems.

It is noteworthy that our modelling approach does not use the divergence correction for the total current density in the form of interspersed iteration steps or additional equations in the system of linear equations (e.g. Smith 1996; Streich 2009). Instead, the goal-oriented approach tries to decrease the normal jumps of current density across element interfaces, in terms of locally adaptive mesh refinement. It honours the continuity of the normal component of the current density solely with an a-posterior error estimator based on this continuity condition. To completely remove the jumps in normal components of current density across interfaces is an ongoing research topic.

From the last high-frequency topographic hill example, the error estimators show large errors in the elements included in the air space due to the strong variations of high-frequency EM waves

Table 2. Parameters of the mesh discretization for *goal-oriented approach J* involving the 3D-1 model at frequencies of 0.1 and 10 Hz. In contrast to the $T-\Omega$ (Mitsuhata & Uchida 2004) and $E-\phi$ (Farquharson & Miensopust 2011) approaches which use structured meshes, we use unstructured meshes.

Frequency	Method	Mesh level	No. elements	No. unknowns	Run time (s)
	Goal-oriented approach J	1	30 835	36 789	10.7
		15	154 572	180 370	107.4
0.1 Hz		20	210 396	245 128	137.9
	$T-\Omega$		18 816	<75 264	
	$E-\phi$		191 100	E (594 199), ϕ (201 640)	
	Goal-oriented approach J	1	73 995	86 451	46.7
		10	320 063	371 972	615.7
10.0 Hz		15	454 846	528 441	946.5
	$T-\Omega$		47 040	<188 160	
	$E-\phi$		191 100	E (594 199), ϕ (201 640)	

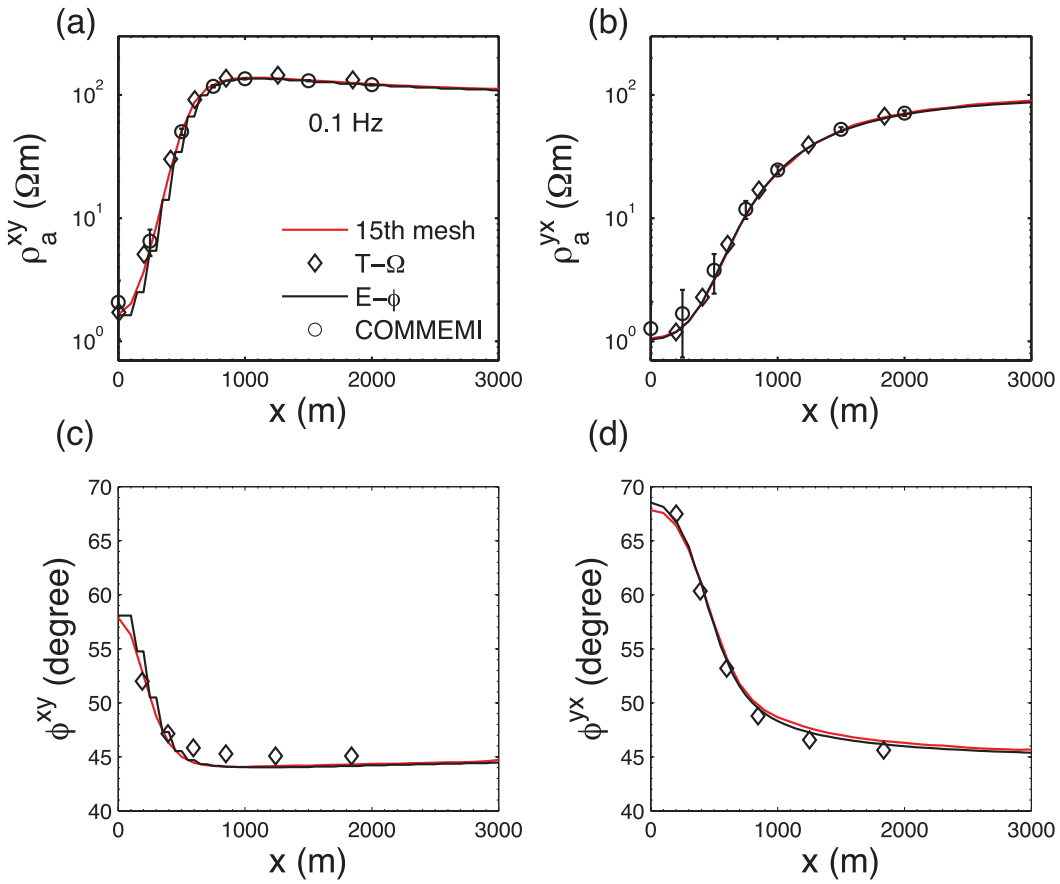

Figure 13. Comparison of apparent resistivities (a and b) and phases (c and d) obtained for FEM meshes of the 15th refinement step by *goal-oriented approach J* to other solutions using different algorithms on the 3D-1 model at a frequency of 0.1 Hz. These reference solutions are from the COMMEMI project (Zhdanov *et al.* 1997), the $T-\Omega$ finite-element solutions on structured meshes (Mitsuhata & Uchida 2004) and the divergence-correction finite-element method (Farquharson & Miensopust 2011) using the curl-curl electrical field equation and structured meshes.

in the air space. This indicates that a nearly global refinement is needed in the air space due to little energy dissipation in the air space. To completely remove the requirements of careful mesh discretization in the air space which is essential at high frequencies, an optimal option is to transform the volume differential equation for the electric field in the air space to a surface integral equation on the topographical surface. Then, we can apply the finite-element method in the Earth domain due to its capability of handling complicated subsurface models. Such a hybrid boundary finite-element approach, which could be very useful for the high-frequency cases, is the subject of our current research and will be reported in a future paper.

ACKNOWLEDGEMENTS

This work was performed in the Applied and Environmental Geophysics Group of ETH Zurich under the overall direction of Prof Dr Alan Green and Prof Dr Johan Robertsson. The research was financially supported by the China Scholarship Council Foundation (2008637007), ETH Zurich and the National Natural Science Foundation of China (40874072). Special thanks are given to Colin G. Farquharson and Yuji Mitsuhata for kindly offering their numerical solutions for comparison. We would like to thank Colin G. Farquharson and another reviewer for valuable comments which significantly improved the manuscript.

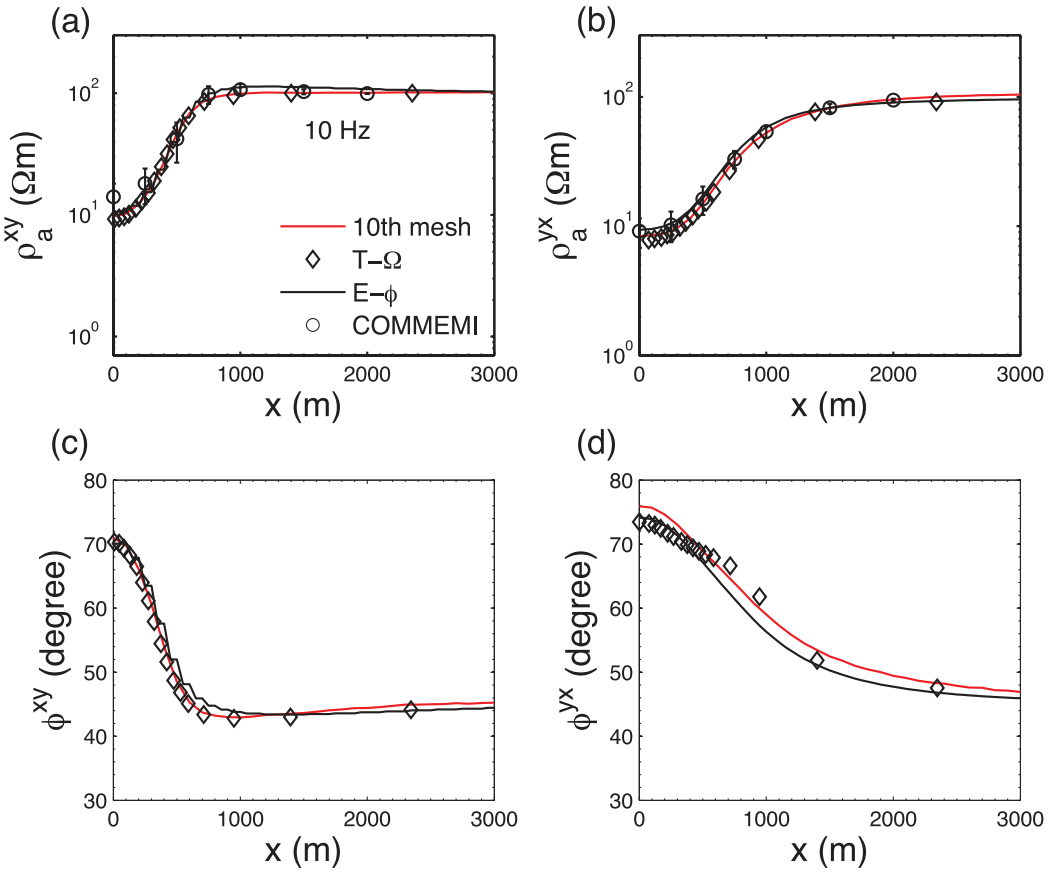

Figure 14. Similar to Fig. 13, but at a frequency of 10 Hz.

REFERENCES

Aprea, C., Booker, J. & Smith, J., 1997. The forward problem of electromagnetic induction: accurate finite-difference approximations for two-dimensional discrete boundaries with arbitrary geometry, *Geophys. J. Int.,* **129,** 29–40.

Avdeev, D., 2005. Three-dimensional electromagnetic modelling and inversion from theory to application, *Surv. Geophys.,* **26,** 767–799.

Avdeev, D., Kuvshinov, A., Pankratov, O. & Newman, G., 2002. Three-dimensional induction logging problems, part I: an integral equation solution and model comparisons, *Geophysics,* **67,** 413–426.

Badea, E., Everett, M., Newman, G. & Biro, O., 2001. Finite-element analysis of controlled-source electromagnetic induction using Coulomb-gauged potentials, *Geophysics,* **66,** 786–799.

Beck, R., Hiptmair, R., Hoppe, R. & Wohlmuth, B., 2000. Residual based a posteriori error estimators for eddy current computation, *Math. Modelling Numer. Anal.,* **34,** 159–182.

Becken, M., Ritter, O., Bedrosian, P. & Weckmann, U., 2011. Correlation between deep fluids, tremor and creep along the central San Andreas fault, *Nature,* **480,** 87–90.

Berdichevsky, M.N. & Dmitriev, V.I., 2008. *Models and Methods of Magnetotellurics,* Springer, Berlin and Heidelberg.

Boerner, R.U., 2010. Numerical modelling in geo-electromagnetics: advances and challenges, *Surv. Geophys.,* **31,** 225–245.

Brenner, S. & Scott, L., 2008. *The Mathematical Theory of Finite Element Methods,* Vol. 15, Springer Verlag, New York.

Chandra, R., Dagum, L., Kohr, D., Maydan, D., MacDonald, J. & Menon, R., 2001. *Parallel Programming in OpenMP,* Morgan Kaufmann, San Francisco.

Chen, L., Booker, J., Jones, A., Wu, N., Unsworth, M., Wei, W. & Tan, H., 1996. Electrically conductive crust in southern Tibet from INDEPTH magnetotelluric surveying, *Science,* **274,** 1694–1696.

Chen, Z., Wang, L. & Zheng, W., 2007. An adaptive multilevel method for time-harmonic Maxwell equations with singularities, *SIAM J. Sci. Comput.,* **29,** 118–138.

Coggon, J., 1971. Electromagnetic and electrical modeling by the finite element method, *Geophysics,* **36,** 132–155.

Doherty, J., 1988. EM modelling using surface integral equations, *Geophys. Prospect.,* **36,** 644–668.

Everett, M., 2011. Theoretical developments in electromagnetic induction geophysics with selected applications in the near surface, *Surv. Geophys.,* **33,** 29–63.

Farquharson, C. & Miensopust, M., 2011. Three-dimensional finite-element modelling of magnetotelluric data with a divergence correction, *J. appl. Geophys.,* **75,** 699–710.

Farquharson, C., Duckworth, K. & Oldenburg, D., 2006. Comparison of integral equation and physical scale modeling of the electromagnetic responses of models with large conductivity contrasts, *Geophysics,* **71**(4), G169–G177.

Franke, A., Borner, R.U. & Spitzer, K., 2007. 3D finite element simulation of magnetotelluric fields using unstructured grids, in *Proceedings of the 4th International Symposium on Three-Dimensional Electromagnetics,* TU Bergakademie Freiberg, Germany.

Franke, A., Boerner, R.U. & Spitzer, K., 2007. Adaptive unstructured grid finite element simulation of two-dimensional magnetotelluric fields for arbitrary surface and seafloor topography, *Geophys. J. Int.,* **171,** 71–86.

Franke, A., Borner, R.U. & Spitzer, K., 2008. Is there a most efficient formulation of the three-dimensional magnetotelluric boundary value problem? in *19th Workshop on Electromagnetic Induction in the Earth,* Beijing, China.

Haber, E., Ascher, U., Aruliah, D. & Oldenburg, D., 2000. Fast simulation of 3D electromagnetic problems using potentials, *J. Comput. Phys.,* **163,** 150–171.

Harrington, R.F., 2001. *Time-Harmonic Electromagnetic Fields,* IEEE Press, New Jersey.

Henderson, A., Ahrens, J. & Law, C., 2004. *The ParaView Guide,* Kitware Clifton Park, NY.

Hohmann, G., 1975. Three-dimensional induced polarization and electromagnetic modeling, *Geophysics,* **40,** 309–324.

Hou, J., Mallan, R.K. & Torres-Verdin, C., 2006. Finite-difference simulation of borehole EM measurements in 3D anisotropic media using coupled scalar-vector potentials, *Geophysics,* **71,** G225–G233.

Intel, 2010. Intel Math Kernel Library, Linear Solver Basics.

Ismail, N. & Pedersen, L., 2011. The electrical conductivity distribution of the Hallandsas Horst, Sweden: a controlled source radiomagnetotelluric study, *Near Surf. Geophys.,* **9,** 45–54.

Jin, J., 2002. *The Finite Element Method in Electromagnetics,* Wiley-IEEE Press, New York.

Kalscheuer, T., Pedersen, L.B. & Siripunvaraporn, W., 2008. Radiomagnetotelluric two-dimensional forward and inverse modelling accounting for displacement currents, *Geophys. J. Int.,* **175,** 486–514.

Key, K. & Ovall, J., 2011. A parallel goal-oriented adaptive finite element method for 2.5-D electromagnetic modelling, *Geophys. J. Int.,* **186,** 137–154.

Key, K. & Weiss, C., 2006. Adaptive finite-element modeling using unstructured grids: the 2D magnetotelluric example, *Geophysics,* **71,** G291–G299.

Li, Y. & Key, K., 2007. 2D marine controlled-source electromagnetic modeling: part 1—an adaptive finite-element algorithm, *Geophysics,* **72,** WA51–WA62.

Liu, E. & Lamontagne, Y., 1998. Geophysical application of a new surface integral equation method for EM modeling, *Geophysics,* **63,** 411–423.

Liu, G. & Becker, A., 1992. Evaluation of terrain effects in AEM surveys using the boundary element method, *Geophysics,* **57,** 272–278.

Mackie, R., Smith, J. & Madden, T., 1994. 3D electromagnetic modeling using finite-difference equations—the magnetotelluric example, *Radio Sci.,* **29,** 923–935.

Mitsuhata, Y. & Uchida, T., 2004. 3D magnetotelluric modeling using the T-Omega finite-element method, *Geophysics,* **69,** 108–119.

Mogi, T., 1996. Three-dimensional modeling of magnetotelluric data using finite element method, *J. appl. Geophys.,* **35,** 185–189.

Nam, M., Kim, H., Song, Y., Lee, T., Son, J. & Suh, J., 2007. 3D magnetotelluric modelling including surface topography, *Geophys. Prospect.,* **55,** 277–287.

Nédélec, J., 1986. A new family of mixed finite elements in R3, *Numer. Math.,* **50,** 57–81.

Nelson, K. *et al.*, 1996. Partially molten middle crust beneath southern Tibet: synthesis of project INDEPTH results, *Science,* **274,** 1684–1688.

Newman, G. & Alumbaugh, D., 2002. Three-dimensional induction logging problems, part 2: a finite-difference solution, *Geophysics,* **67,** 484–491.

Oden, J. & Prudhomme, S., 2001. Goal-oriented error estimation and adaptivity for the finite element method, *Comput. Math. Appl.,* **41,** 735–756.

Olyslager, F., 1994. The behavior of electromagnetic fields at edges in bi-isotropic and bi-anisotropic materials, *IEEE Trans. Antennas Propag.,* **42,** 1392–1397.

Olyslager, F., 1995. Overview of the singular behavior of electromagnetic fields at edges and tips in bi-isotropic and special bianisotropic media, *Radio Sci.,* **30,** 1349–1354.

Parry, J. & Ward, S., 1971. Electromagnetic scattering from cylinders of arbitrary cross section in a conductive half space, *Geophysics,* **36,** 67–100.

Pedersen, L.B., Bastani, M. & Dynesius, L., 2006. Some characteristics of the electromagnetic field from radio transmitters in Europe, *Geophysics,* **71,** G279–G284.

Raiche, A., 1974. An integral equation approach to three-dimensional modelling, *Geophys. J. Int.,* **36**(2), 363–376.

Ren, Z. & Tang, J., 2010. 3D direct current resistivity modeling with unstructured mesh by adaptive finite-element method, *Geophysics,* **75,** H7–H17.

Ren, Z., Kalscheuer, T., Greenhalgh, S. & Maurer, H., 2013. Boundary element solutions for broadband 3D geo-electromagentic problems accelerated by multi-level fast mutlipole method, *Geophys. J. Int.,* **192,** 473–499.

Rücker, C., Günther, T. & Spitzer, K., 2006. Three-dimensional modelling and inversion of DC resistivity data incorporating topography—I. modelling, *Geophys. J. Int.,* **166,** 495–505.

Schenk, O. & Gärtner, K., 2004. Solving unsymmetric sparse systems of linear equations with PARDISO, *Future Gener. Comput. Syst.,* **20,** 475–487.

Schwarzbach, C., Börner, R. & Spitzer, K., 2011. Three-dimensional adaptive higher order finite element simulation for geo-electromagnetics—a marine CSEM example, *Geophys. J. Int.,* **187,** 63–74.

Si, H., 2006. TetGen: a quality tetrahedral mesh generator and three-dimensional Delaunay triangulator, Tech. rep., Weierstrass Institute for Applied Analysis and Stochastic, Berlin, German.

Siripunvaraporn, W., Egbert, G. & Lenbury, Y., 2002. Numerical accuracy of magnetotelluric modeling: a comparison of finite difference approximations, *Earth Planets Space,* **54,** 721–725.

Smith, J., 1996. Conservative modeling of 3-D electromagnetic fields, part II: biconjugate gradient solution and an accelerator, *Geophysics,* **61,** 1319–1324.

Stratton, J., 2007. *Electromagnetic Theory,* Wiley-IEEE Press, New Jersey.

Streich, R., 2009. 3D finite-difference frequency-domain modeling of controlled-source electromagnetic data: direct solution and optimization for high accuracy, *Geophysics,* **74,** F95–F105.

Tezkan, B. & Saraev, A., 2008. A new broadband radiomagnetotelluric instrument: applications to near surface investigations, *Near Surf. Geophys.,* **6,** 245–252.

Wait, J., 1954. On the relation between telluric currents and the Earth's magnetic field, *Geophysics,* **19**(2), 281–289.

Weidelt, P., 1975. Electromagnetic induction in three-dimensional structures, *J. Geophys.,* **41,** 85–109.

Xu, S., Ruan, B., Zhou, H., Chen, L. & Xu, S., 1997. Numerical modeling of 3-D terrain effect on MT field, *Sci. China Ser. D-Earth Sci.,* **40,** 269–275.

Zdunek, A. & Rachowicz, W., 2005. A goal-oriented hp-adaptive finite element approach to radar scattering problems, *Comput. Meth. Appl. Mech. Eng.,* **194,** 657–674.

Zhdanov, M., Varentsov, I., Weaver, J., Golubev, N. & Krylov, V., 1997. Methods for modelling electromagnetic fields: results from COMMEMI—the international project on the comparison of modelling methods for electromagnetic induction, *J. appl. Geophys.,* **37,** 133–271.

Zhdanov, M.S., Lee, S.K. & Yoshioka, K., 2006. Integral equation method for 3D modeling of electromagnetic fields in complex structures with inhomogeneous background conductivity, *Geophysics,* **71,** G333–G345.

Zyserman, F. & Santos, J., 2000. Parallel finite element algorithm with domain decomposition for three-dimensional magnetotelluric modelling, *J. appl. Geophys.,* **44,** 337–352.

APPENDIX A: FINITE-ELEMENT APPROXIMATION

Let Ω be discretized into a set of tetrahedral elements $\mathcal{T} = \bigcup_{n=1}^{N_t} \mathcal{T}_n \subseteq \Omega$, $1 \leq n \leq N_t$, N_t is the total number of tetrahedra. The finite-element approximation is: Seek $\mathbf{E}_h \in H(\mathbf{curl}, \mathcal{T})$, such that

$$B(\mathbf{E}_h, \mathbf{V}_h) = D(\mathbf{V}_h), \quad \forall \mathbf{V}_h \in H(\mathbf{curl}, \mathcal{T}). \tag{A1}$$

Letting the finite-element space $H(\mathbf{curl}, \mathcal{T})$ be reduced to a lowest order curl-conforming linear space $\mathcal{H}(\mathbf{curl}, \mathcal{T})$ (Nédélec 1986) in which only the existence of $\mathbf{V}_h$ and the curl of $\mathbf{V}_h \in \mathcal{H}(\mathbf{curl}, \mathcal{T})$ in the weak sense is guaranteed, the electric field $\mathbf{E}_h \in \mathcal{H}(\mathbf{curl}, \mathcal{T})$ within the discretized computational domain $\mathcal{T}$ can be approximated as

$$\mathbf{E}_h = \sum_{j=1}^{N_e} E_j \mathbf{N}_j, \tag{A2}$$

where E_j is the average tangential electric field along the jth edge in $\mathcal{T}$ and N_e is the total number of edges in $\mathcal{T}$. The lowest order vector Nédélec shape function $\mathbf{N}_j$ (Nédélec 1986) is attached along the jth edge of $\mathcal{T}$. Substituting the above approximation into the weak formulation given by eq. (A1) and selecting the Galerkin test function $\mathbf{V}_h \in \mathcal{H}(\mathbf{curl}, \mathcal{T})$ as $\mathbf{V}_h = \mathbf{N}_i$ to be one of the shape functions used above, we obtain an $N_e \times N_e$ sparse system of linear equations for the electric field

$$\mathbf{A}\mathbf{X}_e = \mathbf{B}. \tag{A3}$$

Here, $\mathbf{X}_e = \{E_j, j = 1, ..., N_e\}$ and the explicit expression for the elements in the system matrix $\mathbf{A}$ is

$$A_{ij} = \iiint_{\Omega} \frac{1}{\xi}(\nabla \times \mathbf{N}_i \cdot \nabla \times \mathbf{N}_j - k^2 \mathbf{N}_i \cdot \mathbf{N}_j)\, \mathrm{d}v. \tag{A4}$$

The source term is given by

$$B_i = \iint_{\partial\Omega} \mathbf{N}_i \cdot \mathbf{g}_t \, \mathrm{d}s. \tag{A5}$$

APPENDIX B: FINITE-ELEMENT APPROXIMATION OF THE DUAL PROBLEM

Using a Galerkin FEM approximation similar to that of the electric field in eq. (A2), we obtain a set of linear equations for the influence field

$$\mathbf{A}\mathbf{X}_w = \mathbf{C}. \tag{B1}$$

Here, $\mathbf{X}_w = \{W_j, j = 1, ..., N_e\}$ and the system matrix is the same as $\mathbf{A}$ in eq. (A4). The source term is given by

$$C_i = \iiint_{\Omega_j} \mathbf{N}_i \cdot \left(\sum_{j=1}^{t} \frac{\mathbf{I}}{V_j} \right) \mathrm{d}v. \tag{B2}$$

Due to $\mathbf{W}_h \in \mathcal{H}(\mathbf{curl}, \mathcal{T})$, the a-posterior error estimators rJH, J and H in eqs (22), (23) and (24), respectively, can be directly applied to the influence field to compute the element error estimators $\eta^w_{T_n}$, which is needed in eq. (30).

APPENDIX C: POST-PROCESSING PROCEDURE

To compute the apparent resistivities and phases from the **E** and **H** fields (as required in MT and RMT applications), we need to solve eq. (A3) with two boundary conditions $\mathbf{g}_t$ on $\partial\Omega$ for at least two different source polarizations, E^p_x and H^p_x, where subscript x denotes the coordinate direction. We assume these independent source fields to correspond to polarized (p) boundary electric and magnetic fields. For the E^p_x source polarization, the boundary electric field E^p is along the x-direction and its amplitude on $\partial\Omega$ at the air side of the flat air–Earth interface is set to one. For the H^p_x source polarization, the boundary magnetic field H^p is along the x-direction and its amplitude on $\partial\Omega$ at the air side of the flat air–Earth interface is set to one. For all other edges on $\partial\Omega$, we compute the necessary boundary values on these of a 1-D layered model with Wait's recursion formula (Wait 1954). The distance to the boundary $\partial\Omega$ from anomalous bodies is set to be 5-10 skin depths where the scattered fields caused by these anomalous bodies can be reasonably ignored (Weidelt 1975; Nam *et al.* 2007).

Assuming that there is a local coordinate system (u, v, n) at each measuring site, the components of the electric fields and magnetic fields are related by an impedance tensor $\mathbf{Z}$ and the vertical magnetic transfer function (VMTF) $\mathbf{T}$ (Berdichevsky & Dmitriev 2008). The impedance tensor is determined as follows:

$$\begin{bmatrix} Z_{uu} & Z_{uv} \\ Z_{vu} & Z_{vv} \end{bmatrix} = \begin{bmatrix} E^{E^p_x}_u & E^{H^p_x}_u \\ E^{E^p_x}_v & E^{H^p_x}_v \end{bmatrix} \begin{bmatrix} H^{E^p_x}_u & H^{H^p_x}_u \\ H^{E^p_x}_v & H^{H^p_x}_v \end{bmatrix}^{-1}. \tag{C1}$$

The VMTF is computed from the expression

$$\begin{bmatrix} T_u \\ T_v \end{bmatrix} = \begin{bmatrix} H^{E^p_x}_u & H^{E^p_x}_v \\ H^{H^p_x}_u & H^{H^p_x}_v \end{bmatrix}^{-1} \begin{bmatrix} H^{E^p_x}_n \\ H^{H^p_x}_n \end{bmatrix}. \tag{C2}$$

Once the impedance tensor is available, the apparent resistivities and phases are extracted from the basic definitions

$$\rho^{ij}_a = \frac{1}{\omega\mu_0}|Z_{ij}|^2, \; i, j = u, v, \tag{C3}$$

$$\phi^{ij} = \arctan\left(\mathrm{Im}(Z_{ij})/\mathrm{Re}(Z_{ij})\right). \tag{C4}$$

SUPPORTING INFORMATION

Additional Supporting Information may be found in the online version of this article:

Figure 1. Illustration of the 3D-2 model of the COMMEMI project (Zhdanov et al. 1997) in the global coordinate (x, y, z) system. The measuring sites are arranged along with the x-axis on the flat air-Earth interface.

Table 1. Computation cost of the 3D-2 model at a frequency of 0.001 Hz.

Figure 2. Comparison of horizontal and vertical components of the magnetic field and horizontal components of the electric field for the 3D-2 model at a frequency of 0.001 Hz for a profile at y=0 m. The solution from the 25th mesh (267,599 unknowns) is convergent to the solution of the 15th mesh (232,262 unknowns).

Figure 3. Comparison of apparent resistivities and phases and vertical magnetic transfer functions (VMTF) for the 3D-2 model at a frequency of 0.001 Hz. The symbol IE stands for solutions obtained by the volume integral equations method (Xiong 1992). The symbol DDFEM stands for solutions obtained by the domain-decomposition finite-element method (Zyserman & Santos 2000). (http://gji.oxfordjournals.org/lookup/suppl/doi:10.1093/gji/ggt154/-/DC1)

Please note: Oxford University Press are not responsible for the content or functionality of any supporting materials supplied by the authors. Any queries (other than missing material) should be directed to the corresponding author for the article.